

1 **Spatial slip rate distribution along the SE Xianshuihe fault, eastern Tibet, and**
2 **earthquake hazard assessment**

3 *Preprint version – content may slightly differ from final publication in TECTONICS*

4 *Original publication:* <https://doi.org/10.1029/2021TC006985>
5

6 Mingkun Bai^{1,2}, Marie-Luce Chevalier^{1,3*}, Philippe Hervé Leloup⁴, Haibing Li^{1,3}, Jiawei Pan^{1,3},
7 Anne Replumaz⁵, Shiguang Wang^{6,1}, Kaiyu Li¹, Qiong Wu¹, Fucui Liu¹, Jinjiang Zhang²

8 ¹ Key Laboratory of Deep-Earth Dynamics of Ministry of Natural Resources, Institute of Geology,
9 Chinese Academy of Geological Sciences, 26 Baiwanzhuang Rd, Beijing 100037, People's
10 Republic of China

11 ² Ministry of Education Key Laboratory of Orogenic Belts and Crustal Evolution, School of Earth
12 and Space Sciences, Peking University, Beijing 100871, People's Republic of China

13 ³ Southern Marine Science and Engineering Guangdong Laboratory (Guangzhou), Guangzhou
14 511458, People's Republic of China

15 ⁴ Laboratoire de géologie de Lyon, CNRS UMR 5570, Université de Lyon, Villeurbanne, France

16 ⁵ ISTERre, Université Grenoble Alpes, CNRS, Grenoble, France

17 ⁶ National Institute of Natural Hazards, Ministry of Emergency Management of China, Beijing,
18 China

19

20 **Highlights**

21 -We determined late Quaternary slip rates of 3.4-4.8 and 9.6-13.4 mm/yr along the Zheduotang and
22 Moxi segments, respectively

23 -We suggest a SE rate increase along the Xianshuihe fault system from Ganzi to Moxi

24 -We discovered a new active fault (Mugecuo South) between Selaha and Zheduotang segments, a
25 large-scale pull-apart within an uplift zone

*Corresponding author : Marie-Luce Chevalier (mlchevalier@hotmail.com), Tel: +86 13466654223

26

27 **Abstract**

28

29 The Xianshuihe (XSH) fault in eastern Tibet is one of the most active faults in China, with
30 the next large earthquake most likely to occur along its SE part, where the fault splits into three
31 parallel branches: Yalahe, Selaha and Zheduotang. Precisely quantifying their slip rates at various
32 timescales is essential to evaluate regional earthquake hazard. Here, we expand our previous work
33 on the Selaha fault to the nearby Zheduotang and Moxi faults, and add observations on the Yalahe
34 fault and on the newly discovered Mugecuo South fault zone. Using tectonic-geomorphology
35 approaches with ^{10}Be dating, we had previously determined average late Quaternary slip rates of
36 9.75 ± 0.15 and 4.4 ± 0.5 mm/yr along the NW and SE Selaha fault, respectively. Using the same
37 methods here, we determine a slip rate of 3.4-4.8 mm/yr on the Zheduotang fault and of 9.6-13.4
38 mm/yr on the Moxi fault. This is consistent with the southeastward slip rate increase we had
39 proposed along the XSH fault system from 6-8 mm/yr (Ganzi fault) to ~ 10 mm/yr (Selaha fault),
40 and >9.6 mm/yr (Moxi fault). We propose a new model for the SE Xianshuihe fault, where the
41 large-scale Mugecuo pull-apart basin lies within an even larger scale compressive uplift zone in a
42 restraining bend of the XSH fault, where the highest peak in eastern Tibet is located (Gongga Shan,
43 7556 m). Our slip rate determination helps to constrain a relatively high regional $M_w\sim 7$ earthquake
44 hazard at present on the SE Xianshuihe fault.

45

46 **Plain Language Summary**

47 The Xianshuihe fault in eastern Tibet is one of the most active faults in China, with the next
48 large earthquake most likely to occur along its southeastern part, where the fault zone consists of
49 four parallel branches with complicated geometries. Studying the activity and slip rate of each
50 branch is essential to evaluate regional earthquake hazard, especially because they cross a major
51 city (Kangding), and because of the imminent construction of the Chengdu-Lhasa railroad. Here, we

52 expand our previous slip rate study on one fault branch (Selaha) to two additional ones (Zheduotang
53 and Moxi), together with key observations on the newly discovered ‘Mugecuo South fault zone’.
54 We find that the rate over the last ~100,000 years may increase southeastwards along the
55 Xianshuihe fault system, as previously suggested. The fast slip rates and their complex spatial
56 distribution in the Kangding region reveal a high earthquake hazard ($M_w \sim 7$) at present.

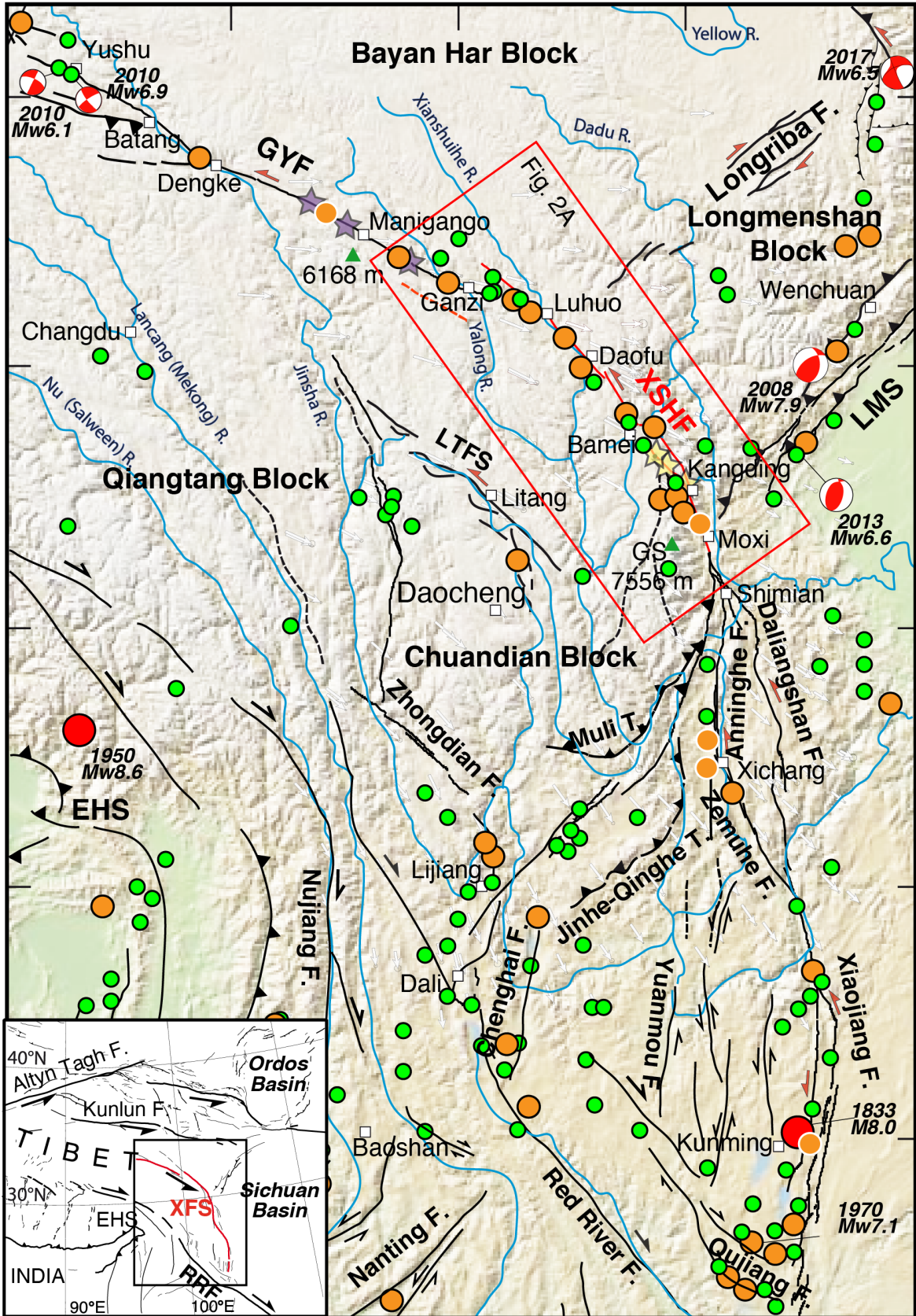
57

58 **1. Introduction**

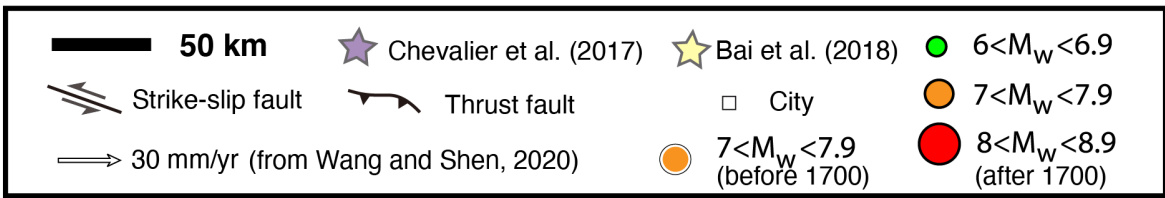
59 The eastern margin of the Tibetan Plateau is an important, active tectonic boundary with
60 numerous active faults which accommodate slip due to the eastward motion of the plateau (e.g.,
61 Tapponnier and Molnar, 1977; Wang et al., 1998; Wang and Burchfiel, 2000; Han et al., 2019) (Fig.
62 1). This region belongs to the “eastern Tibet seismic belt” or “N-S tectonic zone” (Deng et al., 2003;
63 Zhang, 2013) along which an extremely large number of $M > 7$ earthquakes have occurred. In
64 particular, along the NW-striking, ~1400 km-long, left-lateral Xianshuihe (hereafter XSH) fault
65 system, as many as 17 $M > 7$ and 29 $M > 6.5$ earthquakes have occurred along almost its entire length
66 since 1700, with three $M > 7.3$ earthquakes along just the XSH segment since 1923 (Allen et al.,
67 1991; Wen, 2000) (Fig. 2A). Following two large earthquakes nearby (2008 $M_w 7.9$ Wenchuan and
68 2013 $M_s 7$ Lushan, Fig. 1), the seismic risk near Kangding city is believed to have increased by a
69 factor of two, attested by Coulomb stress increase (e.g., Parsons et al., 2008; Toda et al., 2008; Shan
70 et al., 2009, 2013; Nalbant and McCloskey, 2011; Yang et al., 2015; Guo et al., 2018; Xu et al.,
71 2019), which was only partly reduced after the 2014 Kangding earthquake sequence ($M_w 5.9$ and
72 5.6) (Jiang et al 2015a; Bai et al., 2018) (Fig. 2A). The faults of the SE XSH fault region are
73 extremely clear, they cut and offset numerous geomorphic features (moraines, gullies, debris flows,
74 etc.), which are very well-preserved partly due to their remoteness, away from human
75 modifications. In addition, the Kangding region is now widely accepted as a seismic gap (e.g., Allen
76 et al., 1991; Wen, 2000; Wen et al., 2008; Jiang et al., 2015a; Shao et al., 2016; Wang and Shen,
77 2020; Li and Bürgmann, 2021), where a large earthquake would be tragic because of casualties

78 (Kangding city has a population of ~150,000) and infrastructure damage not only due to ground
79 shaking but also because of landslides and mud flows on the very steep surrounding slopes.

96°E 98°E 100°E 102°E 104°E

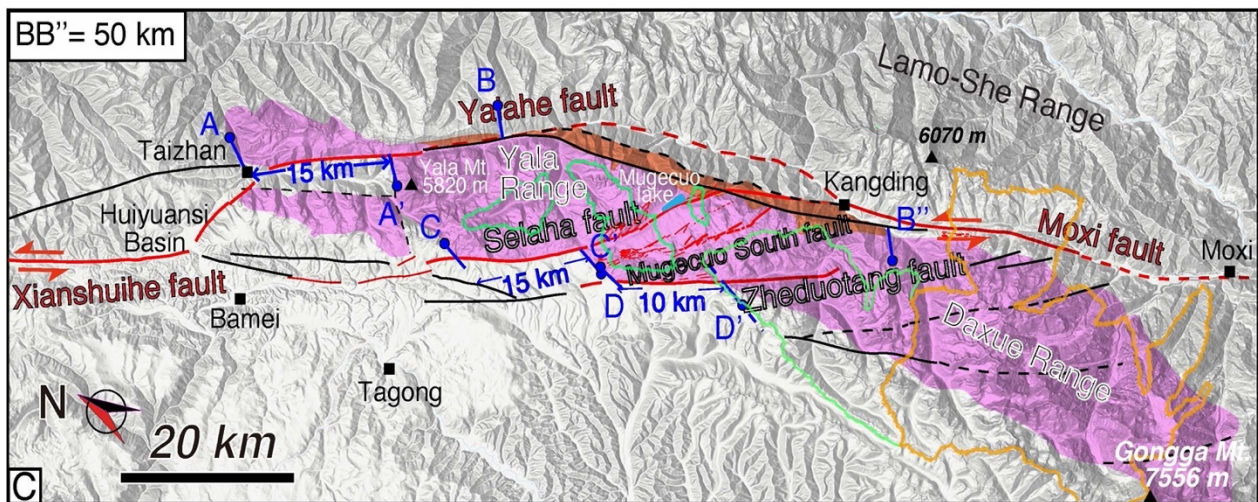
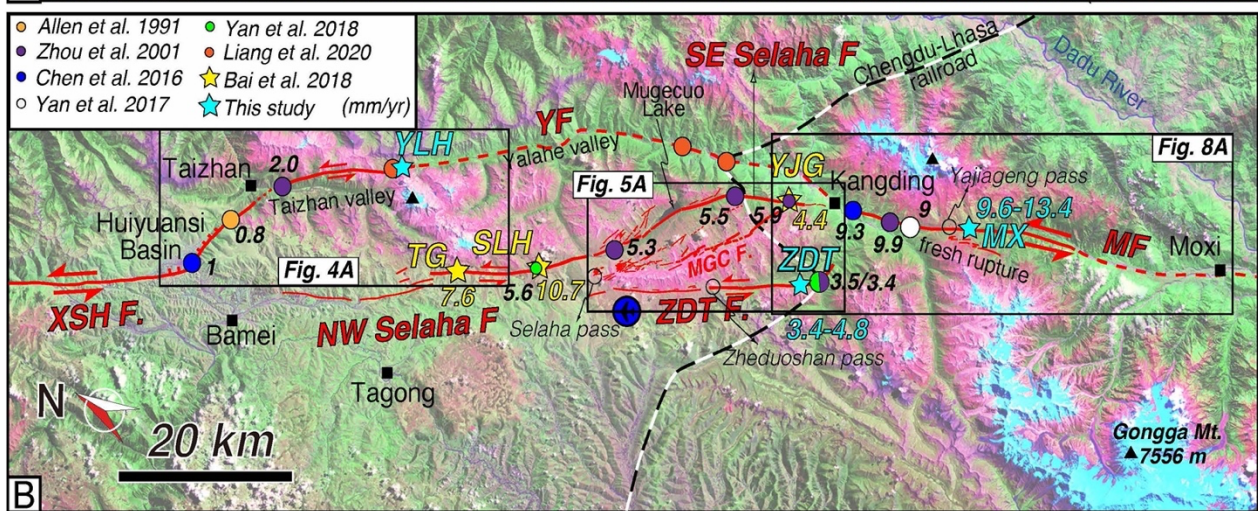
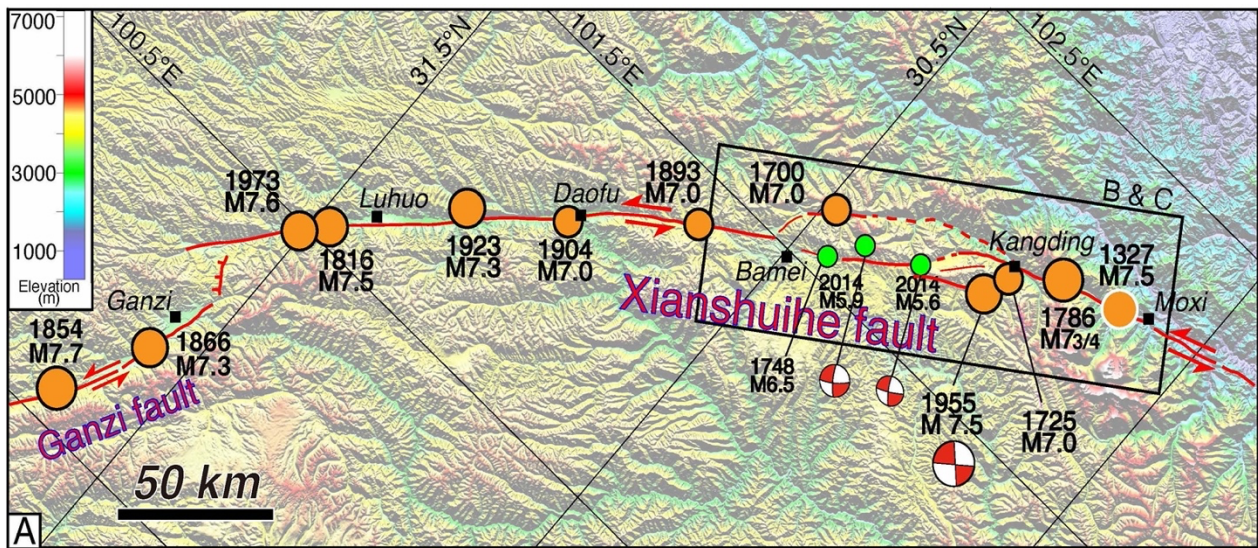


33°N
31°N
29°N
27°N
25°N



81 **Figure 1:** *Xianshuihe fault system (XFS) within India–Asia collision zone. Tectonic map of SE Tibet*
82 *with digital elevation model (DEM) in background. Purple and yellow stars locate study sites from*
83 *Chevalier et al. (2017) and Bai et al. (2018), respectively. Horizontal GPS velocity field with*
84 *respect to stable Eurasian plate (Wang and Shen, 2020), focal mechanisms of instrumental, $M_w > 6$*
85 *earthquakes (Global Harvard CMT catalog 1976–2020) (2008 Wenchuan, 2010 Yushu, 2013*
86 *Lushan and 2017 Jiuzhaigou), as well as earthquakes from US Geological Survey*
87 *(earthquake.usgs.gov) and CEA (1995), main peaks, cities, active faults (those of Xianshuihe fault*
88 *in red) (modified from Allen et al., 1991 and Bai et al., 2018), tectonic blocks and rivers.*
89 *LMS=Longmenshan, GYF=Ganzi-Yushu fault, XSHF=Xianshuihe fault, LTFS=Litang fault system,*
90 *GS=Gongga Shan. Inset shows the XFS within Asia, EHS=Eastern Himalayan Syntaxis, RRF=Red*
91 *River fault.*

92



93

94 **Figure 2:** Xianshuihe (XSH) fault. (A) Distribution of post 1700 A.D. $M > 7$ earthquakes (+ that of
 95 1327 near Moxi) (e.g., USGS, Wen et al., 2008; Cheng et al., 2011) along XSH and SE Ganzi faults.

96 *Focal mechanisms from Jiang et al. (2015a) and Lin et al. (1986). (B) Landsat satellite image of SE*
97 *XSH fault (box in A), where main trace splays into Yalahe (YF), Selaha (NW and SE) and*
98 *Zheduotang (ZDTF) segments before reconnecting as Moxi fault (MF) farther to SE.*
99 *MGCF=Mugecuo South fault. Location of main geographic and topographic features indicated, in*
100 *addition to approximate location of study sites and late Quaternary (average) slip rates from*
101 *others. (C) Simplified geologic map of SE segment of XSH fault, with Gongga-Zheduoshan*
102 *batholith and its geologic offsets (following Liu et al., 1977; Chen et al., 1985). Green and orange*
103 *contours represent moderate (<0.9 mm/yr) and high (0.9 - 7.6 mm/yr) ¹⁰Be basin-wide erosion*
104 *rates, respectively (Ouimet et al., 2009; Cook et al., 2018).*

105

106 Near Kangding city, the linear XSH fault splits into three right-stepping, en-echelon segments,
107 the Yalahe, Selaha and Zheduotang faults, before reconnecting as the Moxi segment (Fig. 2B). In
108 order to better understand the complicated tectonics of this particularly active region of eastern
109 Tibet, and assess its seismic hazard, precisely constraining the slip-rates of the several regional
110 active fault branches is essential. While Bai et al. (2018) determined the Selaha fault's late
111 Quaternary horizontal slip-rate at three locations, in this paper, we constrain that of two other
112 regional fault segments (Zheduotang and Moxi) using similar approaches. We also present
113 preliminary observations on the activity of the central Yalahe segment, as well as of that of the
114 newly discovered 'Mugecuo South' fault zone located between the Selaha and Zheduotang
115 segments, which documents significant extension. Finally, we discuss the distribution of slip rates in
116 the Kangding region of the SE XSH fault in the framework of eastern Tibet and compare the rates
117 with those from other regional studies at all timescales. We propose a model for the SE XSH fault
118 where a large-scale pull-apart basin (Mugecuo) lies within an even larger scale restraining bend
119 where the highest peak in eastern Tibet is located (Gongga Shan, 7556 m), and assess regional
120 seismic hazard using the slip rates we determined. Our work also provides valuable data (new fault
121 discovered, detailed mapping of known fault strands and precise slip rates) to the highly challenging
122 Chengdu-Lhasa railroad construction, which will cross all fault segments discussed here (Fig. 2B).

123

124 **2. Geological setting**

125 The XSH fault system consists of four main left-lateral strike-slip fault segments which
126 separate the Bayan Har and Qiangtang/Chuandian blocks to the NE and SW, respectively: the
127 Yushu/Batang faults at the NW end (where the 2010 M_w 6.9 Yushu earthquake occurred), the Ganzi
128 fault in the NW, the XSH and Moxi faults in the center, and the Anninghe-Zemuhe-Xiaojiang faults
129 in the SE (Fig. 1). In the Kangding region, the surface traces of the Yalaha, Selaha and Zheduotang
130 faults appear to coincide with left-lateral offsets of the Gongga-Zheduoshan granite batholith (Chen
131 et al., 1985) (Fig. 2C) and may be connected at depth (e.g., Allen et al., 1991; Jiang et al., 2015a; Li
132 et al., 2020). While the Selaha and Zheduotang faults show evidence of recent activity along most
133 of their traces, with numerous scarps, sag ponds, and left-lateral (with minor vertical) offsets of
134 mostly moraines and gullies, such clear evidence seemed to be lacking along the Yalaha fault where
135 it is parallel to the Selaha fault (Allen et al., 1991; Bai et al., 2018).

136

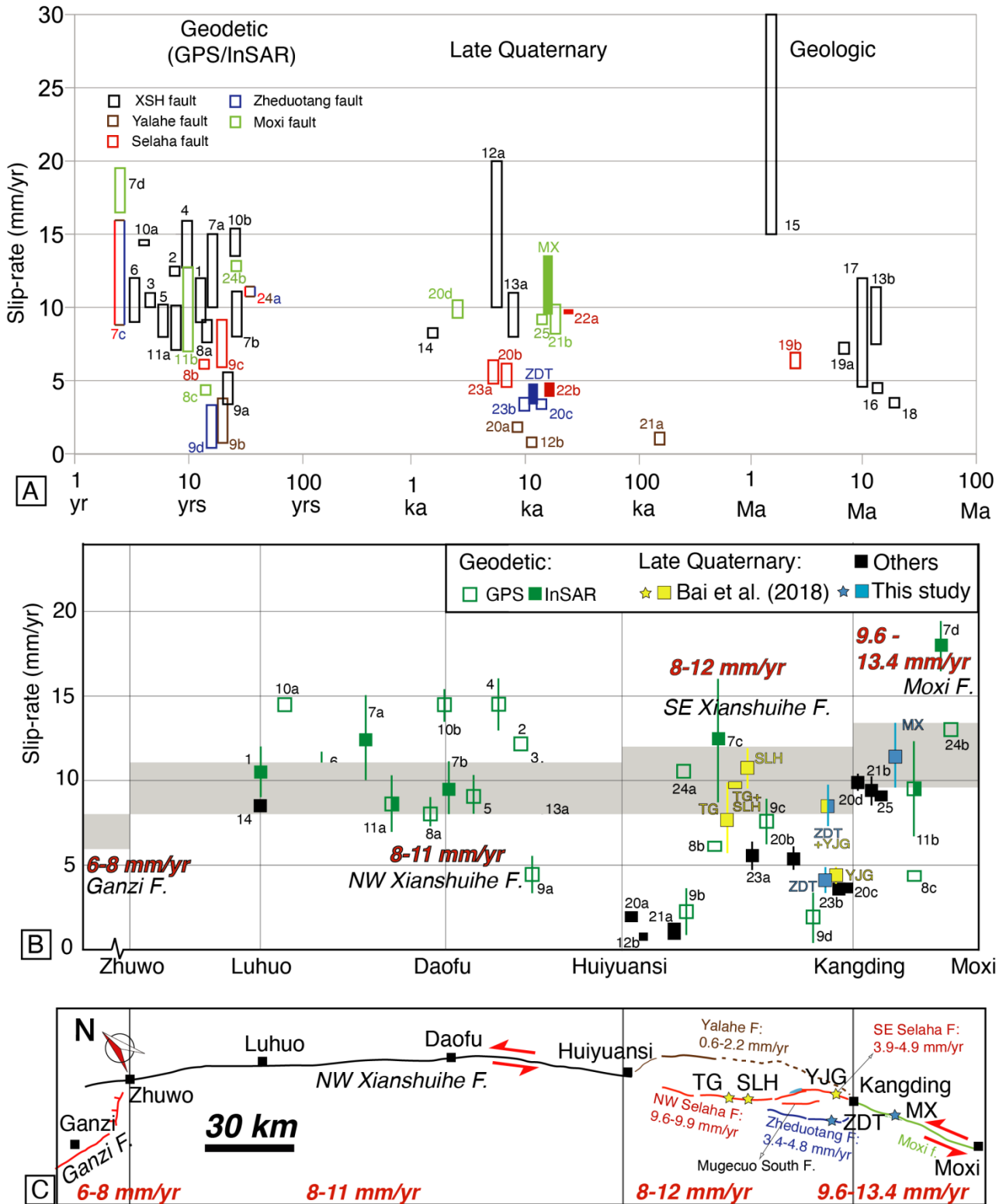
137 **2.1. Slip rates review**

138 As slip rates may vary temporally and/or spatially along a particular fault (e.g., Friedrich et
139 al., 2003; Chevalier et al., 2005), it is important to estimate them at various timescales as
140 summarized below as well as in Figure 3 and Table 1, from a few tens of years (using geodetic
141 techniques such as GNSS [Global Navigation Satellite System] or InSAR [Interferometric Synthetic
142 Aperture Radar]), to a few tens of ka (using tectonic-geomorphology approaches), to a few Ma
143 (using geologic tools).

144 **2.1.1. Geologic timescale**

145 Geologic rate estimates along the XSH fault vary between \sim 3.5 and 30 mm/yr, depending on
146 whether the \sim 60 km geologic offset of several markers (Jinsha and Xianshui Rivers, Proterozoic and
147 Permo-Triassic basement rocks, main Cenozoic thrusts) (e.g., Wang et al., 1998; Wang and
148 Burchfiel, 2000; Yan and Lin, 2015) is matched with initiation ages that vary from 2 to 19 Ma (e.g.,

149 Roger et al., 1995; Wang et al., 1998; Wang et al., 2012; Zhang, 2013; Yan and Lin, 2015; Zhang et
 150 al., 2017).
 151



152
 153 **Figure 3:** Summary of left-lateral slip rates along Xianshuihe and Moxi faults versus time (A) and
 154 location along strike (B). See Table 1 for references to numbers. Colors represent rates along

155 different segments. Filled bars represent our rates (this study as well as that of Bai et al., 2018). (B)
 156 Grey shaded areas represent the best constrained late Quaternary rates for each main section of the
 157 XSH fault: Ganzi, NW XSH, SE XSH, and Moxi faults (see discussion section). (C) Fault trace,
 158 main cities and location of our study sites (blue stars: this study; yellow stars: Bai et al., 2018),
 159 with best constrained late Quaternary slip rates in red at bottom of figure (that of Ganzi from
 160 Chevalier et al., 2017). See text for details.
 161

162 **Table 1: Slip rate summary along Xianshuihe fault**

Segment	Slip-rate (mm/yr)	Reference	Method	Ref. in Fig. 3
XSH fault	9 - 12	Wang et al. (2009)	InSAR near Luhuo	1
	12.2 - 13	W. Wang et al. (2017)	GPS - block model	2
	10 - 11	Shen et al. (2005)	GPS - rigid blocks	3
	12.7 - 15.9	Y. Wang et al. (2017)	GPS - block model	4
	8 - 10.2	Zheng et al. (2017)	GPS - profiles	5
	9 - 12	Ji et al. (2020)	InSAR - interseismic deformation	6
	10 - 15	Zhang et al. (2019)	InSAR - dislocation model	7a
	8.1-11.1	Qiao and Zhou (2021)	InSAR	7b
	7.67 - 9.13	Li et al. (2019)	Gravity + GPS (Luohuo-Qianning)	8a
	3.4 - 5.6	Li et al. (2020)	GPS + earthquake relocation (Daofu-Qianning)	9a
	14.4	Gan et al. (2007)	GPS - dislocation	10a
	13.6-15.4	Wang et al. (2020)	GPS - elastic block model	10b
	7 - 10.3	Jiang et al. (2015b)	3D visco-elastic model with InSAR and GPS data	11a
	10 - 20	Allen et al. (1991)	inferred ages	12a
	8 - 11	Zhang (2013)	reinterpretation of Chen et al. (2008), using upper terrace age	13a
	8.4	Liang et al. (2020)	¹⁴ C - Paleoequake 3 ka (Luhuo)	14
	7.5 - 11.1	Zhang (2013)	90 - 100 km in 10 Ma	13b
	15 - 30	Wang et al. (1998)	60 km in 2-4 Ma	15
	~4.5	Roger et al. (1995)	62 km in 13 Ma (Bai et al., 2018)	16
	4.6 - 12	Yan and Lin (2015)	62 km in 5-13 Ma	17
~3.5	Wang et al. (2012)	62 km in 17±2 Ma (Bai et al., 2018)	18	
6.8 - 7.6	Zhang et al. (2017)	62 km since 8.6±0.5 Ma	19a	
Yalaha fault	0.8 - 3.8	Li et al. (2020)	GPS + earthquake relocation	9b
	0.8	Allen et al. (1991)	inferred ages	12b
	1.8 - 2.2	Zhou et al. (2001)	one TL age - paleoseimology	20a
	0.6 - 1.5	Chen et al. (2016)	TL ages - tectonic geomorphology	21a
Selaha fault	6.14	Li et al. (2019)	Gravity + GPS data	8b
	5.9 - 9.1	Li et al. (2020)	GPS + earthquake relocation	9c
	4.9 - 6.1	Zhou et al. (2001)	TL and ¹⁴ C ages - paleoseimology	20b
	9.6 - 9.9	Bai et al. (2018)	¹⁰ Be (TG and SLH sites, NW Selaha fault)	22a
	3.9 - 4.9	Bai et al. (2018)	¹⁰ Be (YJG site, SE Selaha fault)	22b
	4.8 - 6.4	Yan et al. (2018)	¹⁴ C - tectonic geomorphology	23a
5.7 - 6.9	Zhang et al. (2017)	25 km since 4±0.4 Ma (Bai et al., 2018)	19b	
Zheduotang fault	0.4 - 3.4	Li et al. (2020)	GPS + earthquake relocation	9d
	3.2 - 3.8	Zhou et al. (2001)	¹⁴ C - paleoseimology	20c
	3 - 3.8	Yan et al. (2018)	¹⁴ C - tectonic geomorphology	23b
	3.4 - 4.8	This study	¹⁰ Be (ZDT site)	ZDT
Yalaha/Selaha/Zheduotang	~11	Wang and Shen (2020)	GPS - profiles	24a
	8.8-16	Qiao and Zhou (2021)	InSAR	7c
Moxi fault	7 - 12.7	Jiang et al. (2015b)	3D visco-elastic model with InSAR and GPS data	11b
	4.41	Li et al. (2019)	Gravity and GPS data	8c
	~13	Wang and Shen (2020)	GPS - profiles	24b

16.5-19.3	Qiao and Zhou (2021)	InSAR	7d
9.3 - 10.5	Zhou et al. (2001)	¹⁴ C - paleoseimology	20d
8.3 - 10.3	Chen et al. (2016)	¹⁴ C - tectonic geomorphology	21b
~9	Yan et al. (2017)	¹⁴ C - paleoseimology	25
9.6 - 13.4	This study	¹⁰Be (MX site)	MX

163

164 2.1.2. Late Quaternary timescale

165 A growing body of evidence now suggests a slip rate of ~10 mm/yr for the XSH fault (e.g.,
166 Zhang, 2013; Bai et al., 2018). Bai et al. (2018) suggested that the southeastward rate increase
167 between the Ganzi fault (~6-8 mm/yr, Chevalier et al., 2017) and the XSH fault may be linked to
168 interaction with the nearby NE-striking, reverse/dextral Longriba fault system to the north, as
169 endorsed by a recent GPS study (Wang et al., 2020). The Longriba fault indeed marks the limit
170 between the fast-moving Bayan Har block to the NW and the slow-moving Longmenshan block to
171 the SE, as observed in GPS data when considered relative to stable Eurasia (e.g., W. Wang et al.
172 2017, 2020; Y. Wang et al., 2017; Wang and Shen, 2020) (Fig. 1).

173 What occurs in the Kangding region, however, where the fault splits into three segments, is
174 more complex. While the NW Yalahe fault, with a normal/left-lateral sense consistent with its
175 oblique direction compared to the general trend of the fault, may slip at ~0.6 to 2.2 mm/yr (Allen et
176 al., 1991; Zhou et al., 2001; Chen et al., 2016; Figs. 2B, 3, and Table 1), no rates have yet been
177 determined farther to the SE. Along the NW Selaha fault (west of the Selaha Pass, Fig. 2B), slip
178 rates had been inferred to range between 3.7 and 9.7 mm/yr (Allen et al., 1991; Chen et al., 2016)
179 and were estimated (using ¹⁴C dating) as ranging from 4.8 to 6.4 mm/yr (Zhou et al., 2001; Yan et
180 al., 2018). More recently, Bai et al. (2018) studied two sites along the NW Selaha fault (TG and
181 SLH) and one site along its SE part (YJG) (yellow stars in Fig. 2B). Using ¹⁰Be dating and offset-
182 age reconstructions, they determined slip-rates of 7.6(+2.3/-1.9) mm/yr at TG and 10.7(+1.3/-1.1)
183 mm/yr at SLH, hence 9.6 - 9.9 mm/yr assuming that the rate should be similar at these two sites
184 located only 9 km apart. At YJG, located along the SE Selaha fault, Bai et al. (2018) determined a
185 much lower rate of 3.9 - 4.9 mm/yr. This led them to infer a rate of ~5 mm/yr on the parallel

186 Zheduotang fault, corresponding to the difference between rates along the NW and SE Selaha fault.
187 Other studies on the Zheduotang fault have suggested slip-rates of 3 to 3.8 mm/yr using radiocarbon
188 dating from Zheduotang village towards the SE termination of the fault (Zhou et al., 2001; Yan et
189 al., 2018) (Figs. 2B, 3, and Table 1). However, these rates need to be taken with caution because of
190 the lack of detailed mapping and reported information about the samples, which were not collected
191 exactly where the offsets were estimated.

192 The linear and continuous ~50 km-long Moxi fault, located SE of Kangding, merges with the
193 Selaha fault (Allen et al., 1991; Jiang et al., 2015a; Bai et al., 2018). Previous studies have used ^{14}C
194 dating from trenches located <9 km from Kangding, NW of the Yajiageng (or Xuemenkan) Pass
195 (Fig. 2B), to determine late Quaternary slip-rates along the Moxi fault of ~8.3-10.5 mm/yr (e.g.,
196 Zhou et al., 2001; Chen et al., 2016; Yan et al., 2017). Here, using a different technique
197 (cosmogenic dating), we focus on the segment located SE of the pass.

198 **2.1.3. Geodetic timescale**

199 At the geodetic timescale, InSAR-derived (7-15 mm/yr, e.g., Wang et al., 2009; Jiang et al.,
200 2015b; Zhang et al., 2019; Ji et al., 2020; Qiao and Zhou, 2021) and GPS-derived (8-15.9 mm/yr,
201 e.g., Shen et al. 2005; Gan et al., 2007; W. Wang et al., 2017, 2020; Y. Wang et al., 2017; Zheng et
202 al., 2017; Li et al., 2019) rates along the XSH fault (Fig. 3 and Table 1) are widespread but
203 encompass the late Quaternary rates. The XSH fault slip rate based on the longest GPS record is
204 slightly lower at ~8 to 10.2 mm/yr (Zheng et al., 2017). At a more detailed level, GPS-derived rates
205 vary between 0.8 and 3.8 mm/yr along the Yalahe fault (Li et al., 2020), 5.9-9.1 mm/yr along the
206 Selaha fault (Li et al., 2019; Li et al., 2020), 0.4-3.4 mm/yr along the Zheduotang fault (Li et al.,
207 2020) and 4.41-19.3 mm/yr along the Moxi fault (Jiang et al., 2015b; Li et al., 2019; Wang and
208 Shen, 2020; Qiao and Zhou, 2021). Two recent studies have suggested rates of ~11 mm/yr (Wang
209 and Shen, 2020) and 8.8-16 mm/yr (Qiao and Zhou, 2021) across the three branches
210 (Yalahe/Selaha/Zheduotang) of the SE XSH fault (Fig. 3 and Table 1).

211

212 2.2. Past earthquakes in the Kangding region

213 One M7.0 earthquake in 1700 has been reported along the Yalahe fault with ~41 km of surface
214 ruptures (Wen, 2000; Wen et al., 2008) (Fig. 2A). Two historical earthquakes, M7.0 in 1725 and
215 M6.5 in 1748, have both been inferred to have ~40 km of surface ruptures along the SE and NW
216 Selaha fault, respectively, the former being however poorly constrained (Wen, 2000; Wen et al.,
217 2008; Papadimitriou et al., 2004). The recent 2014 M_w 5.9 and 5.6 Kangding earthquake sequence
218 also mostly shook the NW part of that fault (e.g., Jiang et al., 2015a). Along the Zheduotang fault,
219 the 1955 M_w 7.5 Kangding earthquake produced 35 km of surface ruptures (Wen, 2000; Wen et al.,
220 2008; Zhou et al., 2001; Papadimitriou et al., 2004), although it has recently been re-evaluated by
221 Yan et al. (2019) as only M_w 7.0 with 43 km of surface ruptures that extend farther SE towards Moxi
222 (labeled as ‘fresh rupture’ in Fig. 2B). Along the Moxi fault, two M7.5 and $M_{7.5}$ earthquakes
223 occurred in 1327 and 1786, respectively, the latter having produced 70-90 km of surface ruptures
224 and 2-5 m of co-seismic offsets (Zhou et al., 2001; Wen et al., 2008; Cheng et al., 2011). The 1786
225 earthquake also yielded a landslide dam across the nearby Dadu River, whose rupture ten days later
226 following a strong aftershock caused one of the most disastrous landslide dam failures in the world
227 with ~100,000 casualties (e.g., Dai et al., 2005).

228

229 3. Methods

230 We used field investigation as well as Google Earth and Bing high-resolution satellite
231 imagery to map active fault strands and offset geomorphic features along the Zheduotang and Moxi
232 fault segments of the SE XSH fault near Kangding. We could then select the best sites with limited
233 signs of erosion and clear piercing points across the fault in order to precisely measure the
234 cumulative offsets. In this high elevation and high-relief region (with slopes up to 35° along the
235 Zheduotang fault and 15° along the Moxi fault at our study sites), moraines and gullies are the most
236 commonly observed offset markers, in addition to related sag ponds and fault scarps. Good sites are
237 scarce. We selected the best two sites along the fault segments to conduct our study: the Zheduotang

238 (ZDT) and Moxi (MX) moraines. Their crests are sub-rounded and oblique to the fault, resulting in
239 larger offset uncertainties, so that offsets were measured on high-resolution Digital Elevation
240 Models (DEM) obtained from Unmanned Aerial Vehicle (UAV, DJI Phantom 4 Pro) surveys at both
241 sites, and from additional surveys using a Riegel VZ1000 terrestrial LiDAR (Light Detection and
242 Ranging) (angular resolution of 0.02° for raw data, set to 0.5 m between two data points after
243 process) at the MX site. Offset values and their uncertainties were obtained by repeatedly realigning
244 the offset moraine crests to their best original fit on the DEM. Note that along a left-lateral fault,
245 offset of the lateral moraine located to the left (looking downstream) of the gully or stream in
246 between the pair of lateral crests, best represents the total offset, as that to the right may suffer
247 continuous lateral erosion thus only yielding a minimum offset.

248 We use cosmogenic ^{10}Be surface-exposure dating (e.g., Lal, 1991; Gosse and Phillips, 2001)
249 to constrain the moraine abandonment ages following mineral separation and quartz cleaning
250 procedure modified from Kohl and Nishiizumi (1992). ^{10}Be concentrations mostly come from
251 nuclide accumulation from exposure to cosmic rays at the site. We collected a total of 20 samples
252 along the crests on the left bank: nine samples from the lateral moraine crest at the ZDT site and 11
253 from that at the MX site. These samples come from the top few centimeters of large, stable, well-
254 embedded granite boulders (1-5 m in diameter, Figs. S1-S2) using chisel and hammer. Collecting
255 numerous (>6) samples on individual moraine crests has long been shown (Chevalier et al., 2011;
256 Chevalier and Replumaz, 2019) to greatly increase the likelihood of dating the actual age of
257 moraine abandonment (because moraines can only become stable after the ice retreats, hence what
258 we date is the onset age of deglaciation). Ideally, one wants to sample boulders that have been
259 exposed on moraine crests since the onset of deglaciation, with no rolling, shielding or surface
260 erosion since deposition (which would tend to skew the ages toward values younger than the actual
261 age), and no exposure prior to deposition (which would tend to skew the ages toward older values).
262 These old ages, however, are occasional (e.g., Hallet and Pukonen, 1994; Putkonen and Swanson,
263 2003; Heyman et al., 2011) and may be singled out and discarded using statistical tests such as

264 Chauvenet (Bevington and Robinson, 2002) or Peirce criteria, because they have a low probability
265 of belonging to the same population as the rest of the data set. One may apply the criteria several
266 times, while maintaining a statistically sound number of samples left in the data set, however
267 stopping after three iterations in cases of continuously scattered distributions (Chevalier et al.,
268 2016). Four (three young and one old) outliers were found on the MX crest and two old outliers
269 were found on the ZDT crest (Table S1). After rejecting them and following Heyman (2014), we
270 assign a Class B (for moderately-clustered ages) to each moraine, using reduced Chi-square
271 analyses (also see Chevalier and Replumaz, 2019). The oldest age of the age distribution (after
272 rejecting the outliers) is then taken to represent the most likely abandonment age the moraines
273 (Heyman, 2014).

274 Samples were processed at the National Institute of Natural Hazards, Ministry of Emergency
275 Management of China (Beijing), and $^{10}\text{Be}/^9\text{Be}$ ratios were measured at GNS Science (New
276 Zealand). Model ages were calculated using CRONUS v3 (Balco et al., 2008) with the Lm (Lal
277 [1991]/Stone [2000], time-dependent) and LSDn (Lifton et al., 2014, time-dependent) production
278 rate models (Table 2) and we refer to the Lm ages in the text for easier comparison with Bai et al.
279 (2018). No erosion rate and no correction for potential snow and vegetation covers were applied.
280 Therefore, the apparent ages we calculate are minimum ages. We then assign a marine oxygen
281 isotope stage (MIS) (e.g., Lisiecki and Raymo, 2005) to each moraine, which indicates the climatic
282 period during which the moraine was abandoned. Eventually, we combine the moraine
283 abandonment ages with their offsets to reconstruct the space-time evolution of the Zheduotang and
284 Moxi faults and determine their late Quaternary average slip-rates. We report the latter as median
285 rates (with uncertainties at the 68.27% confidence interval about the median) obtained using the
286 Gaussian uncertainty model of Zechar and Frankel (2009).

287

288 **4. Site descriptions and results**

289 We describe the faults and study sites from NW to SE along the SE XSH fault (Fig. 2B).

290 First, we introduce our preliminary results attesting to the central Yalahe fault activity, just north of
291 Yala Mountain (Fig. 4), then describe the newly discovered 'Mugecuo South' fault zone (Fig. 5)
292 located on the NE flank of the Zheduoshan Range between the Selaha and Zheduotang faults. We
293 then present the two study sites, the ZDT moraine along the Zheduotang fault (Figs. 6, 7) and the
294 MX moraine along the Moxi fault (Figs. 7, 8).

295

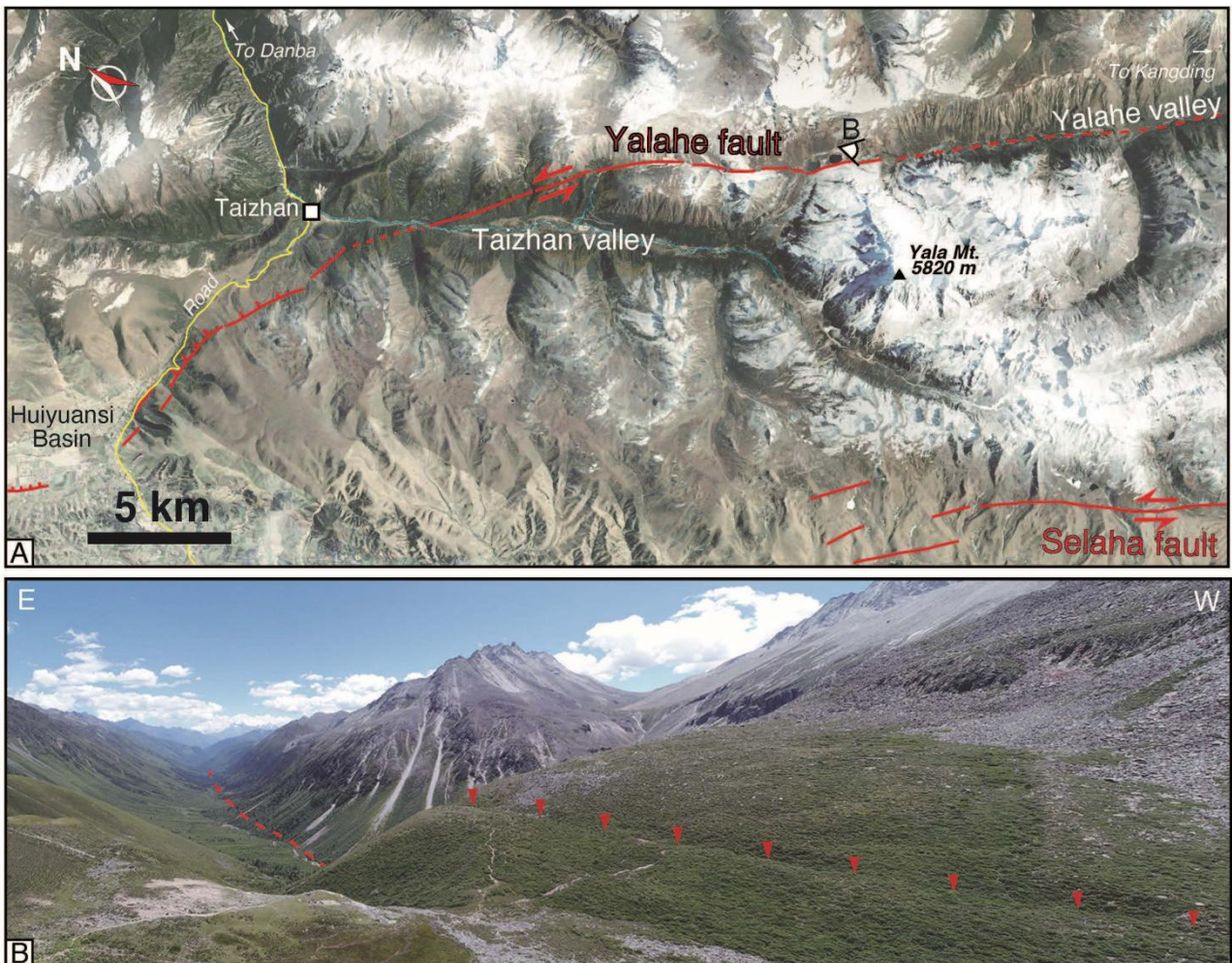
296 **4.1. Yalahe fault**

297 The Yalahe fault constitutes the NE branch of the right-stepping, en-echelon faults of the
298 active SE XSH fault (Fig. 2B). It runs from the eastern Huiyuansi Basin where it strikes N108°E,
299 cuts across the slopes of Taizhan valley then strikes N141°E along the northern side of Yala
300 Mountain, from where it more or less follows the Yalahe valley for ~18 km until it reaches
301 Kangding city (Fig. 2B,C). The Yalahe geologic fault extends ~130 km NW of Taizhan before
302 merging with the XSH fault. Near Taizhan, the Gongga-Zheduoshan granite batholith is affected by
303 a ~1.3 km-wide zone of ductile and brittle deformation linked to the left-lateral Yalahe fault (Chen
304 et al., 1985). The northern boundary of the batholith shows an apparent minimum offset of 15 km
305 (A-A' in Fig. 2C), but the offset of the southern boundary may be as large as 50 km (B-B'' in Fig.
306 2C) (Bai et al., 2018).

307 The active NW part of the Yalahe fault bounds the SE Huiyuansi Basin, which was created
308 thanks to the significant oblique (left-lateral/normal) component of motion along that segment, in
309 agreement with its oblique strike direction compared to that of the main XSH fault (e.g., Allen et al.
310 1991) (Fig. 2B). Aerial photograph analyses (Allen et al., 1991) and field investigation (Liang et al.,
311 2020) show that the central part of the fault between ~Taizhan and Yala Mountain has a clear trace
312 suggesting that it is also active. The fault can be followed for ~7 km on satellite images, and during
313 our own field investigation, we followed a ~1 m-high fault scarp for another ~2.4 km (Fig. 4). Liang
314 et al. (2020) found several co-seismic (2.5-3.5 m) as well as one cumulative (~15 m) horizontal
315 offsets along that central section. Just SE of Yala Mountain however, in the large U-shaped Yalahe

316 valley (Fig. 4B), the fault trace cannot easily be followed on satellite images, either because this
317 section may be inactive at present with activity having been transferred to the Selaha fault (e.g.,
318 Zhang et al., 2017; Bai et al., 2018), or because of the dense vegetation making remote sensing
319 analyses difficult. Extra field work is clearly necessary to constrain the behavior of the Yalaha fault
320 along its SE section. While Allen et al. (1991) found no evidence of the Yalaha fault closer to
321 Kangding city, most likely due to the numerous villages in that valley hindering precise aerial
322 mapping due to human modifications, Liang et al. (2020) found in three naturally exposed sections
323 (Fig. 2B) that the active Yalaha fault cuts through gravel strata underneath radiocarbon-dated, early
324 to mid-Holocene alluvial surfaces.

325



326
327 **Figure 4:** Yalaha fault. (A) Google Earth image of Yalaha fault between Huiyuansi Basin and
328 Yalaha valley. Legend as in Figure 1. (B) View looking south along fault, with clear, linear, ~1 m-
329 high scarp. Farther SE, fault trace becomes hard to follow (dashed line).

330

331 **4.2. Selaha fault and Mugecuo pull-apart**

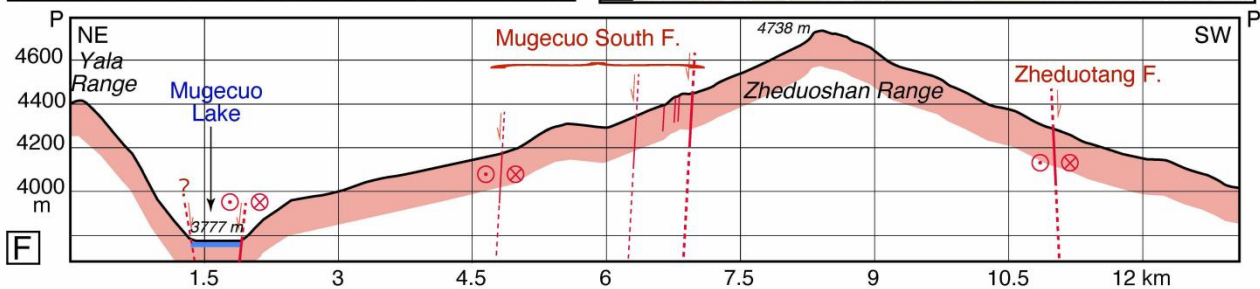
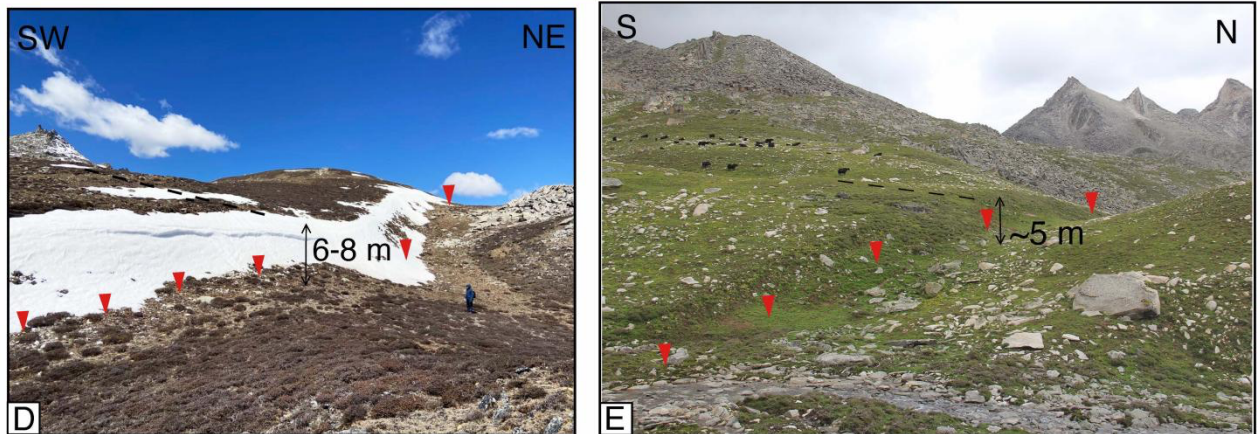
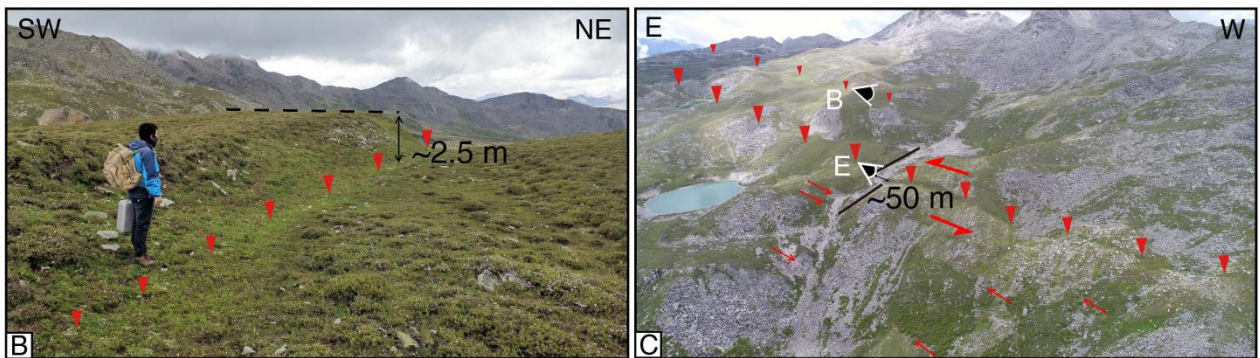
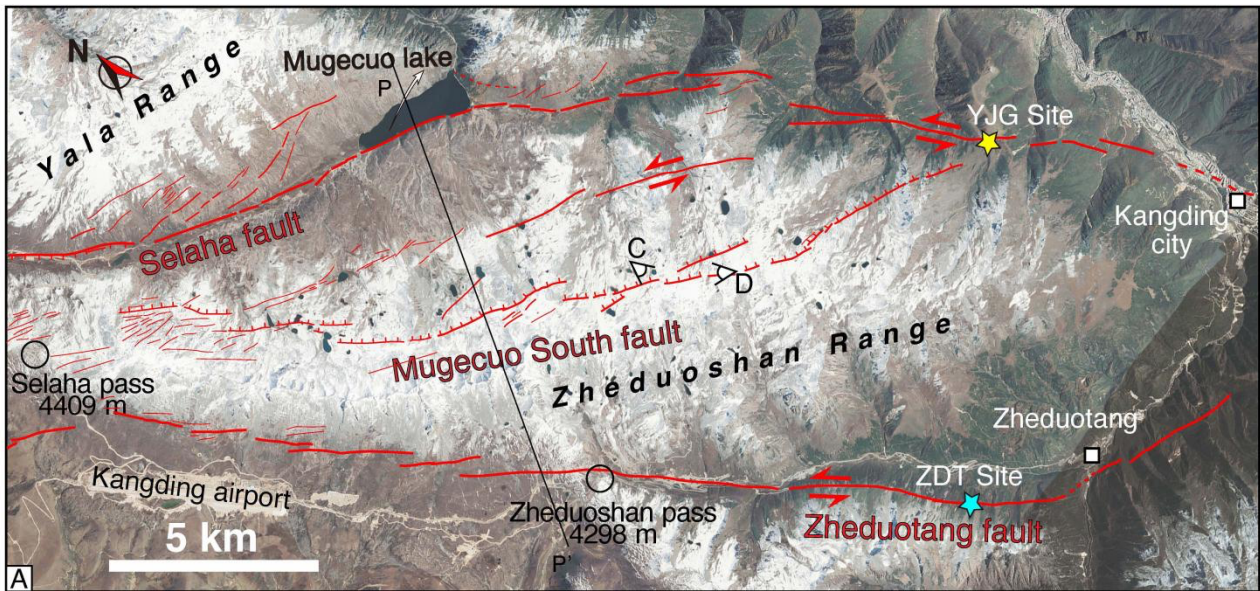
332 While the Selaha fault was suggested as the main active branch of the SE XSH fault (Bai et
333 al., 2018), its trace between the Selaha Pass and Mugecuo Lake is not as clear as that farther NW
334 and SE (Fig. 2B). To the NW, morphological evidence for active faulting abounds along a linear
335 N144°E trend where the TG and SLH sites of Bai et al. (2018) are located (Fig. 2B), following the
336 geological fault that separates the Gongga-Zheduoshan batholith from Triassic sediments (Chen et
337 al., 1985) (Fig. 2C). It is along that fault that the M_w 5.6 and M_w 5.9 Kangding earthquakes occurred
338 in 2014. These earthquakes exhibit purely strike-slip focal mechanisms with a nodal plane striking
339 N139°-143°E for the first one and N148°-152°E for the second one (Jiang et al., 2015a), i.e.,
340 parallel to the NW Selaha fault (Fig. 2A). The fault left-laterally offsets the batholith's western edge
341 by ~15 km (Roger et al., 1995; Bai et al., 2018) (CC' in Fig. 2C). To the SE, the fault is continuous
342 and linear again, trending N154°, where Bai et al. (2018)'s YJG site is located (Fig. 5A). Between
343 these two linear fault splays, the strike of the Selaha fault is however N116°E for ~14 km, where
344 Mugecuo Lake lies. This segment probably has an important normal component and defines a
345 releasing bend (Allen et al., 1991; Bai et al., 2018). However, the precise geometry and individual
346 fault traces in that releasing bend were not clearly documented until now.

347 The ~600 m-high (Fig. 5F), steep topographic slope marking the north side of Mugecuo
348 Lake (Yala Range) most likely corresponds to the morphological expression of a recent normal fault
349 trending N116°E and is cut by several topographic scarps that we interpret as secondary faults (Fig.
350 5A). South of the lake, the NE slopes of the Zheduoshan Range are less steep but our UAV (Fig.
351 5C) and field (Fig. 5B,D,E) surveys revealed numerous ~N110°-140°E-trending topographic scarps
352 up to ~10 m-high, in a ~22 km-long, ~3 km-wide, ~N120°E zone (Pan et al., 2020). We interpret
353 these scarps as the morphological expression of active normal faults constituting the 'Mugecuo
354 South fault zone' (Pan et al., 2020), which not only confirm that the Mugecuo Lake area is a
355 releasing bend between the two linear splays of the Selaha fault, but also show that it is a 14x4.5 km

356 pull-apart basin with Mugecuo Lake located at its lowest point (Figs. 2B and 5A,F).

357 While Wen (2000) and Wen et al. (2008) inferred, following Li et al. (1997), that the M7.0
358 1725 earthquake produced ~35 km of surface ruptures along the SE Selaha fault, with maximum co-
359 seismic offsets of ~3.5 m, we however, infer that this earthquake may have occurred on the
360 Mugecuo South fault zone, which was unknown until now. This is partly due to the fresher nature of
361 the scarps with free-faces (dip $>70^\circ$, Fig. 5B) at places along the Mugecuo South fault zone,
362 compared to those along the SE Selaha fault, although not as fresh as those from the 1955
363 earthquake on the Zheduotang fault.

364



365
 366 **Figure 5:** Mugecuo South fault zone and releasing bend. (A) Google Earth image of Selaha,
 367 Zheduotang and Mugecuo South faults between Selaha Pass and Kangding. Legend as in Figures 1
 368 and 2. (B,D,E) Field photos of fault scarps along Mugecuo South fault zone. (C) UAV photo of
 369 faults from Mugecuo South fault zone highlighted by red triangles and arrows. Note left-lateral

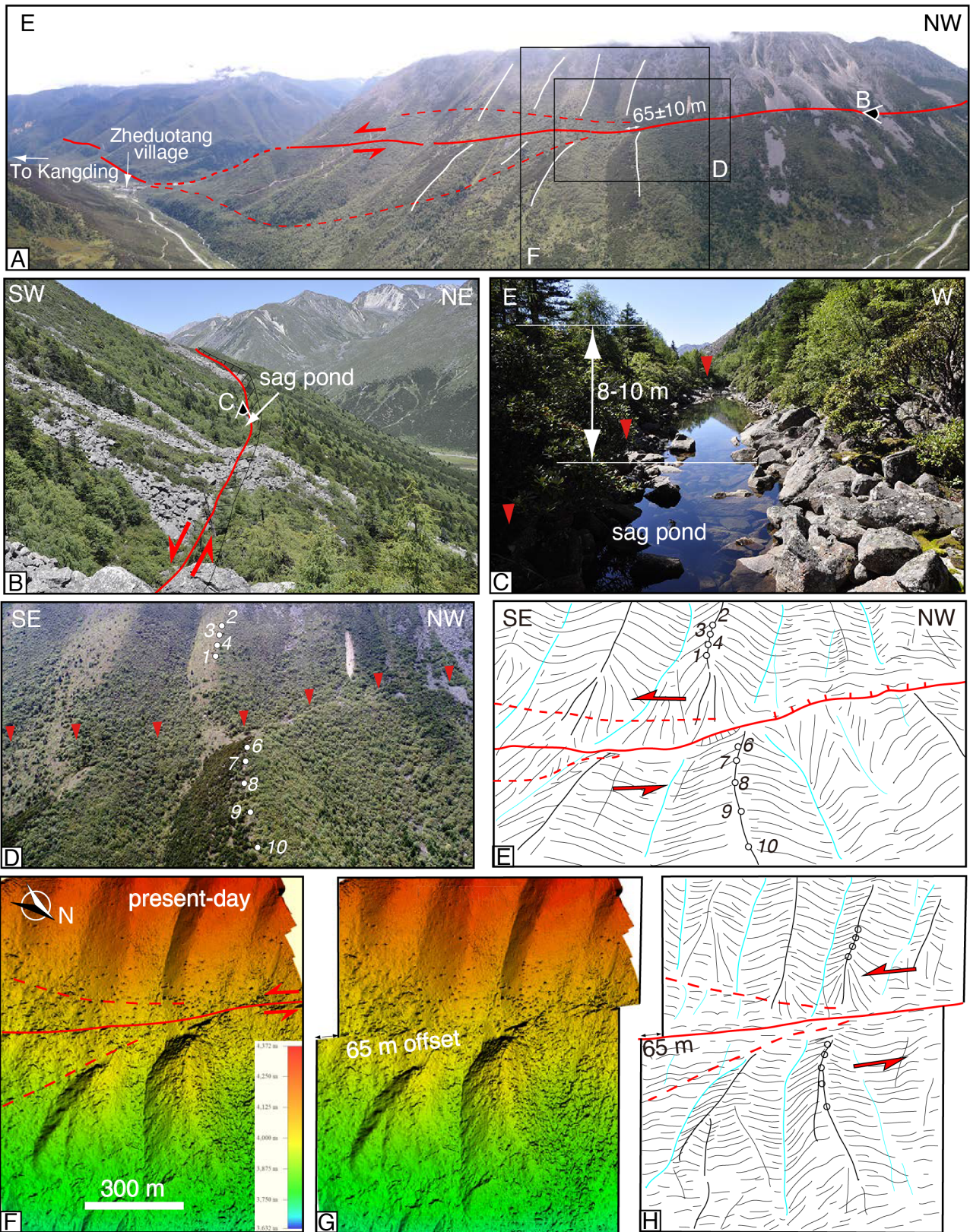
370 *offset. (F) Topographic profile across Mugecuo pull-apart and Zheduoshan Range. Recent faults in*
371 *red, dashed where unknown.*

372

373 **4.3. Zheduotang fault and ZDT site**

374 South of the Mugecuo pull-apart, the ~27 km-long, N148°-striking Zheduotang fault left-
375 laterally offsets the western boundary of the Gongga-Zheduoshan batholith by ~10 km (Bai et al.,
376 2018) (DD' in Fig. 2C). The fault follows the SW-facing slopes of the Zheduoshan Range for ~13
377 km, from Kangding airport to the Zheduoshan Pass, before becoming hard to follow in the valley
378 due to the Kangding-Lhasa highway. The fault becomes clear again once it reaches the steep (~35°),
379 NE-facing mountain slopes, on which numerous rockslides are present (Figs. 5A and 6A,B,D). It is
380 along that section that the fault best displays left-lateral offsets of moraines (Fig. 6A,D). The fault
381 has a slight normal component of motion with SW (uphill)-facing scarps, resulting in numerous sag
382 ponds along the fault, particularly impressive along the section between the highway and
383 Zheduotang village where the scarps can reach 8-10 m-high (Fig. 6B,C). That section ruptured
384 during the 1955 M_w 7.5 earthquake that shows a purely left-lateral focal plane (N137°E, dip 89° to
385 SW) (Lin et al., 1986) that is roughly parallel to the fault trace (N148°E) (Fig. 2A). Farther to the
386 SE, the Zheduotang fault changes direction to become ~N95°, reaches the valley again at
387 Zheduotang village and cuts the mountain slopes for another ~2 km before it becomes hard to
388 follow (Fig. 6A).

389

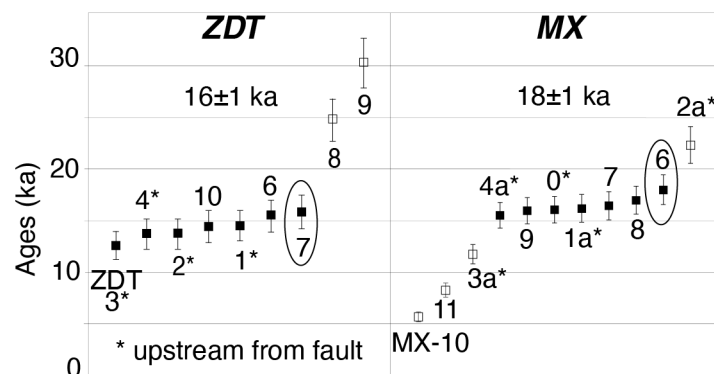


390

391 **Figure 6:** Zheduotang fault and ZDT site. (A) Panoramic UAV photo of SE segment of Zheduotang
 392 fault with white lines highlighting offset moraine crests. Red dashed lines are inferred fault traces.
 393 (B) Photo of uphill-facing fault scarp along which numerous sag ponds are present. (C) Photo of
 394 uphill-facing, 8-10 m-high, fault scarp. (D,E) UAV photo of ZDT moraine with white circles and
 395 numbers representing ^{10}Be samples (ZDT-1 to 10), and its interpretation. (F,G) Present-day and

396 offset reconstruction of 65 ± 10 m offset on LiDAR DEM obtained from our UAV surveys. (H)
 397 Interpretation of G.
 398

399 The Zheduotang (ZDT) moraines are located ~ 10 km due west of the city of Kangding, at
 400 ~ 3860 m of elevation (Figs. 2B and 6). Their sub-rounded crests are ~ 1 km-long and are covered
 401 with medium-sized granite boulders (~ 1 m diameter) (Fig. S1). While the upper crest is only
 402 covered with small bushes and occasional trees, the lower crest is covered with denser vegetation,
 403 especially on its NW-facing slope (Fig. 6D). The Zheduotang fault cuts and left-laterally offsets the
 404 ZDT moraines by 65 ± 10 m (Figs. 6F-H). The steep slopes, extremely dense vegetation at lower
 405 elevations, numerous rockslides with very large, angular boulders, and the large stream at the base
 406 of the mountain slopes, all made this site extremely challenging to reach. We were nevertheless able
 407 to collect a total of nine samples from the NW crest: four upstream from the fault (ZDT-1-4) and
 408 five downstream (ZDT-6-10) (Fig. 6D). Ages range from 12.7 ± 1.0 ka to 30.0 ± 2.4 ka (Fig. 7 and
 409 Table 2). Applying statistical tests (see method section) allows to discard the two oldest samples,
 410 with the remaining seven samples being moderately-clustered (moraine is Class B), ranging from
 411 12.7 ± 1.0 to 15.9 ± 1.2 ka. Therefore, the oldest age is taken to represent the moraine's abandonment
 412 age. Combining offset and age yields a left-lateral slip-rate of 4.1 ± 0.7 mm/yr, or a range of slip rate
 413 between 3.4 and 4.8 mm/yr.



414

415 **Figure 7:** ^{10}Be cosmogenic surface-exposure ages of the ZDT and MX moraines, calculated using
 416 CRONUS v3 (Balco et al., 2008), with 'Lm' production rate model (Lal (1991)/Stone (2000) time-
 417 dependent model). Outliers (open symbols) were discarded using Chauvenet and Peirce criteria
 418 (see method section for details and Table S1). Oldest ages (circled) are indicated.

Sample name	Lat (°N)	Long (°E)	Elev.	shielding	¹⁰ Be(at/g)	Lm ages (yrs)	Internal Uncertainties	LSDn ages (yrs)	Internal Uncertainties
ZDT site									
upstream									
ZDT-1	30.007218	101.853394	3938	0.97	582604±9527	14523±1132	241	14815±922	246
ZDT-2	30.007075	101.852399	4024	0.97	569669±11427	13748±1083	280	13920±881	283
ZDT-3	30.007142	101.852666	3998	0.97	506680±9258	12655±990	234	12908±808	239
ZDT-4	30.007173	101.853023	3954	0.97	544843±12160	13643±1083	309	13863±888	314
downstream									
ZDT-6	30.008677	101.855455	3818	0.97	588013±11776	15418±1217	314	15771±1000	321
ZDT-7	30.00863	101.855689	3813	0.97	604810±11605	15863±1249	310	16259±1027	318
ZDT-8#	30.008681	101.856037	3831	0.97	1018291±17250	24910±1968	434	25226±1591	439
ZDT-9#	30.009041	101.856574	3796	0.97	1222029±15333	30046±2360	389	30494±1901	395
ZDT-10	30.00918	101.856736	3779	0.97	534327±9037	14453±1129	248	14817±924	255
Moxi site									
upstream									
MX-0	29.88182	102.009519	3877	0.99	644968±14438	16099±1282	373	16434±1056	382
MX-1a	29.881898	102.009739	3879	0.99	651371±19511	16231±1334	504	16556±1115	516
MX-2a#	29.881799	102.00999	3879	0.99	941220±19057	22354±1779	472	22654±1448	479
MX-3a#	29.881875	102.01018	3868	0.99	448416±10022	11810±936	273	12148±777	281
MX-4a	29.881813	102.010269	3870	0.99	620232±14033	15559±1240	365	15905±1022	374
downstream									
MX-6	29.883161	102.011295	3865	0.99	726534±15952	18029±1437	411	18470±1186	421
MX-7	29.883558	102.010804	3887	0.99	666039±21318	16481±1368	548	16866±1153	560
MX-8	29.880397	102.011228	3881	0.99	686869±13617	17022±1345	350	17392±1103	358
MX-9	29.882661	102.012665	3862	0.99	636352±12761	16002±1264	333	16361±1038	340
MX-10#	29.882107	102.0135603	3838	0.99	196027±6791	5748±478	204	6031±415	214
MX-11#	29.879169	102.016253	3777	0.99	290547±8810	8329±680	260	8714±584	273

422 Ages are calculated with the CRONUS v3 calculator (Balco et al., 2008). Sample names with # represent outliers that
 423 were statistically rejected (see text). All samples are granite (density 2.7 g/cm³). Thickness is 5 cm.

424 No erosion rate was applied. Standard used at GNS is '01-5-4', with ¹⁰Be/⁹Be = 2.851e-12.

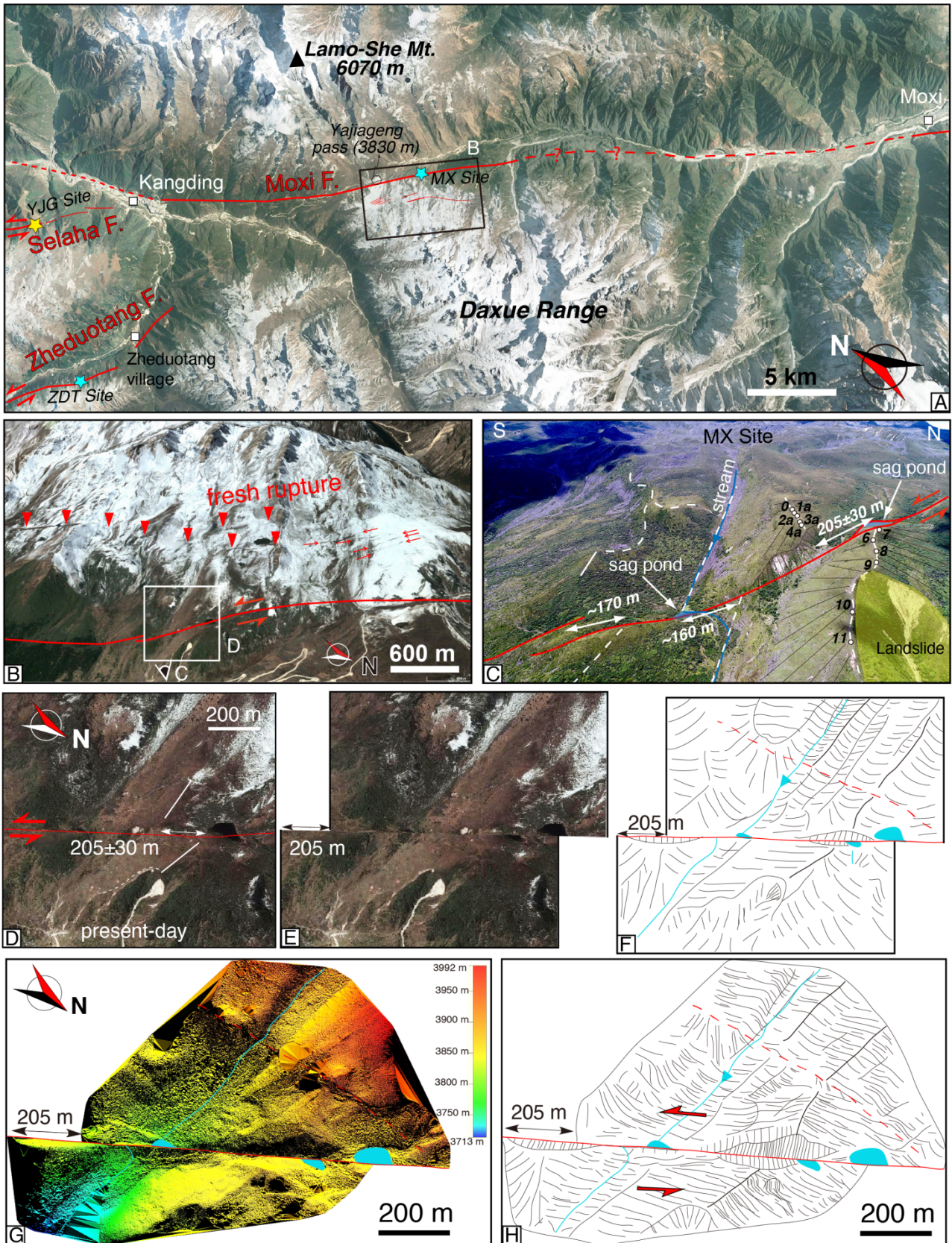
425 Lm=Lal (1991)/Stone (2000) time-dependent production rate model; LSDn=Lifton et al. (2014) production rate model.

426

427 4.4. Moxi fault and MX site

428 The NNW-striking Moxi fault runs from Kangding to Moxi cities (Fig. 2B,C), lying between
 429 the Proterozoic Kangding igneous complex and slivers of Paleozoic rocks (Lu et al., 1975; Liu et al.
 430 1977). The fault shows evidence of recent faulting along its northern section where it cuts through
 431 the western slopes of the Lamo-She Range, crosses the Yajiageng (or Xuemenkan) Pass (3830 m)
 432 then cuts through the eastern slopes of the Daxue Range (where Gongga Shan lies) (Fig. 8A). The
 433 fault is very clear, with numerous offset moraines, gullies, and alluvial fans, forming sag ponds at
 434 places thanks to its slight normal component of motion, with NE-facing scarps north of the pass and
 435 SW-facing scarps to the south. While the main Moxi fault lies quite low on the mountain slopes,
 436 numerous other fault strands are present higher on the slopes near the Yajiageng Pass ('fresh
 437 rupture' in Fig. 8A,B) (Yan et al., 2019), with W to SW-facing scarps damming sag ponds. Farther
 438 SE, the fault trace becomes harder to follow because it reaches the Moxi valley, which is filled with

439 large streams (coming directly from Gongga Shan), very large fluvio-glacial terraces and rockslide
 440 deposits.



441
 442 **Figure 8:** Moxi fault and MX site. (A) Google Earth image of Moxi, SE Zheduotang and Selaha
 443 faults. Legend as in Figures 1 and 2. (B) Google Earth 3D image of fresh surface ruptures parallel

444 *to Moxi fault, located ~1 km to the west. Note the 180° rotation between panels A and B. (C) UAV*
445 *photo interpretation of MX moraine. (D,E) Present-day and offset reconstruction of the 205±30 m*
446 *offset on Google Earth image. (F) Interpretation of E. (G) Offset reconstruction of the 205±30 m*
447 *offset on LiDAR DEM obtained from our UAV and LiDAR surveys. (H) Interpretation of H.*
448

449 The ~1.5 km-long Moxi (MX) moraines are located along the segment just SE of the Yajiageng
450 Pass, ~ 15 km SE of Kangding, at ~3850 m elevation (Fig. 8). The MX moraine crests are sub-
451 rounded and covered with small bushes and large granite boulders (Fig. S2). A landslide removed
452 part of the main moraine downstream from the fault (Fig. 8). Thanks to the left-lateral motion on
453 the Moxi fault, two sag ponds have formed at the base of the resulting SW-facing scarps (Fig. 8C),
454 the larger at the base of the northern crest (north of the stream, blue in Fig. 8C). The main northern
455 and southern (i.e., south of the stream) MX moraine crests are left-laterally offset by 205±30 and
456 ~170 m, respectively (Fig. 8). A smaller offset for the southern crest is expected due to the sense of
457 motion of the Moxi fault, with the stream in between, whose offset is ~160 m at present, constantly
458 refreshing the lateral slopes.

459 We collected 11 samples at the MX site along the northern crests, five upstream from the
460 fault (MX-0, MX-1a-4a) and six downstream (MX-6-11) (Fig. 8C). Ages range from 5.7±0.5 to
461 22.3±1.8 ka (Fig. 7 and Table 2). Applying statistical tests allows us to discard the three youngest
462 and the oldest samples. It is interesting to note that the young outliers are located the farthest
463 downstream, most likely reflecting material removal due to the landslide, which has reshaped the
464 crest to its present-day geometry. The original crest may thus only be preserved close to the fault,
465 where samples MX-6 to 9 are located. The seven remaining samples cluster moderately well and the
466 moraine is Class B. Therefore, the oldest age is taken to best represent the moraine's abandonment
467 age, which is 18.0±1.4 ka. Combining the offset and the age of the main, northern moraine yields a
468 left-lateral slip-rate of 11.4(+2.0/-1.8) mm/yr, or a range of 9.6 to 13.4 mm/yr. Note that the 'fresh
469 rupture' (located ~1 km west of the Moxi fault, Fig. 8B) may also absorb part of the deformation,
470 thus the slip rate we determined is a minimum.

471

472 **5. Discussion**

473 **5.1. Late Quaternary slip distribution across the various segments of the SE Xianshuihe fault**

474 Along the NW XSH fault, where the single fault trace is linear and continuous, late
475 Quaternary left-lateral slip rates have been estimated at 8 - 11 mm/yr (#13a, Fig. 3 and Table 1)
476 (Zhang, 2013, reinterpreting Chen et al. (2008)'s data) and ~8.4 mm/yr (#14) (Liang et al., 2020).
477 South of the Huiyuansi Basin, where the XSH fault splits into the Yalahe, Selaha, Mugecuo South
478 and Zheduotang branches, Bai et al. (2018), using the same technique as in this paper, determined
479 rates of 9.6-9.9 (TG+SLH sites, Fig. 3B) and 3.9 - 4.9 mm/yr (YJG site) along the NW and SE parts
480 of the Selaha fault, respectively, since ~20 ka. Our present study at the ZDT site allowed us to
481 determine a late Quaternary (~16 ka) rate of 3.4 - 4.8 mm/yr along the Zheduotang fault. Summing
482 the slip rates along the SE Selaha fault (YJG site) and the Zheduotang fault (ZDT site) yields 7.3-
483 9.7 mm/yr (ZDT+YJG, Fig. 3). This appears to confirm the inference of Bai et al. (2018) that recent
484 motion on the NW Selaha fault is then partitioned between the SE Selaha fault and the parallel
485 Zheduotang fault farther to the SE. However, the total XSH fault slip rate at this longitude should
486 also consider the slip rate on the Yalahe fault, although it has been estimated to be quite low, and
487 only from its NW part where its normal component is important (Figs. 2B and 4A). It was first
488 qualitatively inferred as ~0.8 mm/yr (#12b, Fig. 3 and Table 1) (Allen et al., 1991), before being
489 constrained at 1.8 - 2.2 mm/yr since 10 ka (#20a) (Zhou et al., 2001) and 0.6 (since 10-15 ka) to 1.5
490 (since 70 ka) mm/yr (#21a) (Chen et al., 2016) from thermoluminescence ages. Therefore, assuming
491 similar rates of 0.6-2.2 mm/yr along the SE Yalahe fault, and in the absence of reported quantitative
492 measurements, the total late Quaternary slip rate across the Yalahe, SE Selaha and Zheduotang
493 branches becomes >7.9-11.9 mm/yr. Note that this rate is a minimum because the rate along the
494 Mugecuo South fault is currently unknown.

495 Along the Moxi fault, we determined a slip rate of 9.6 - 13.4 mm/yr since ~18 ka at the MX
496 site. Previously published rates (Zhou et al., 2001; Chen et al., 2016; Yan et al., 2017) range from

497 8.3 to 10.5 mm/yr at the northern extremity of the fault (Fig. 3 and Table 1). These three studies
498 used ^{14}C dating mostly in trenches dug across the fault. While this method may allow to accurately
499 constrain the age of individual earthquakes, it is not the most accurate for determining slip rates
500 along strike-slip faults because horizontal offsets are difficult to measure in such trenches.

501 From NW to SE, the late Quaternary slip rates along the XSH fault system thus appear to
502 increase progressively from $\sim 6 - 8$ mm/yr along the Ganzi fault (Chevalier et al., 2017), $\sim 8 - 11$
503 mm/yr along the single-stranded NW XSH fault (Zhang, 2013, Liang et al., 2020), $>8 - 12$ mm/yr
504 across the Yalahe / Selaha / Mugecuo / Zheduotang faults (e.g., Bai et al., 2018, this study), to 9.6-
505 13.4 mm/yr along the Moxi segment (Figs. 3B,C and 9).

506

507 **5.2 Comparison with geodetic rates**

508 Comparison between our late Quaternary rates and geodetic ones is not straightforward, in
509 part due to the still limited number of regional GPS stations north of the XSH fault. The two latest
510 publications based on GPS data have adopted different strategies.

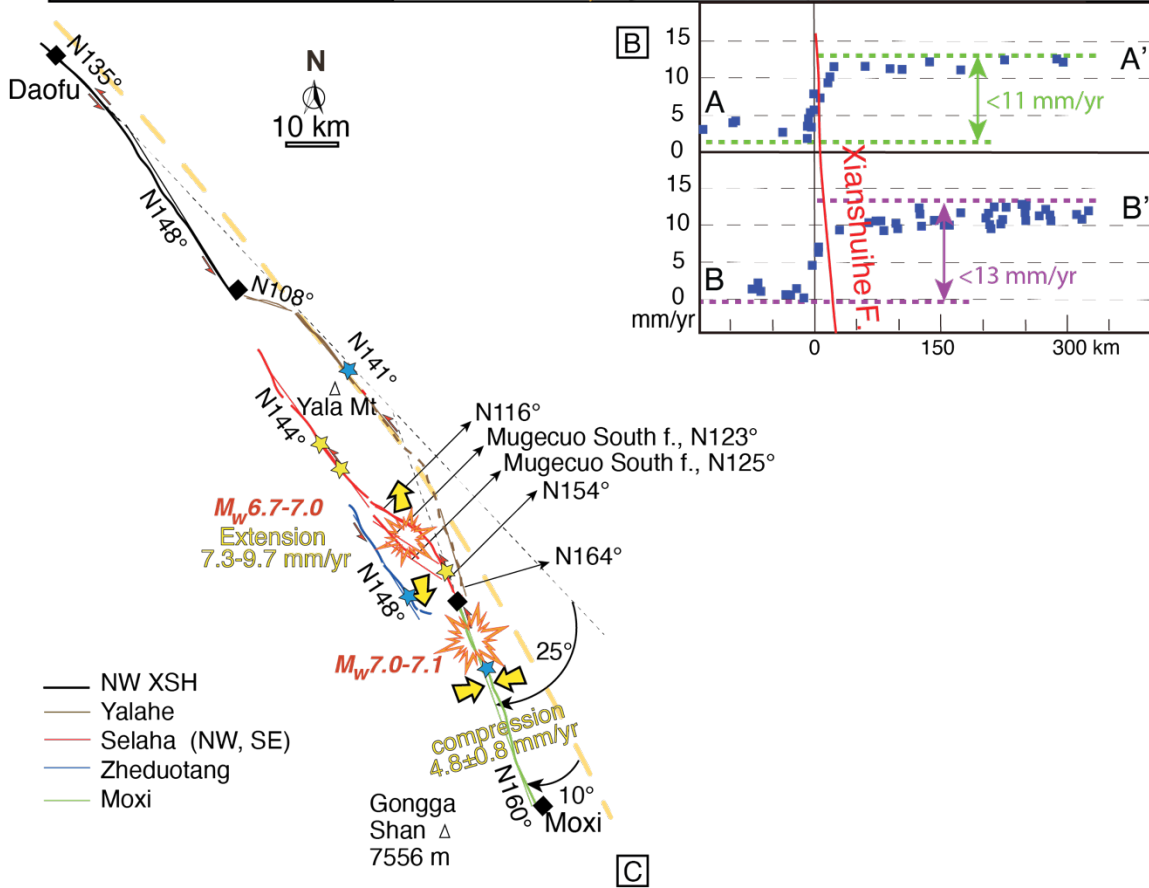
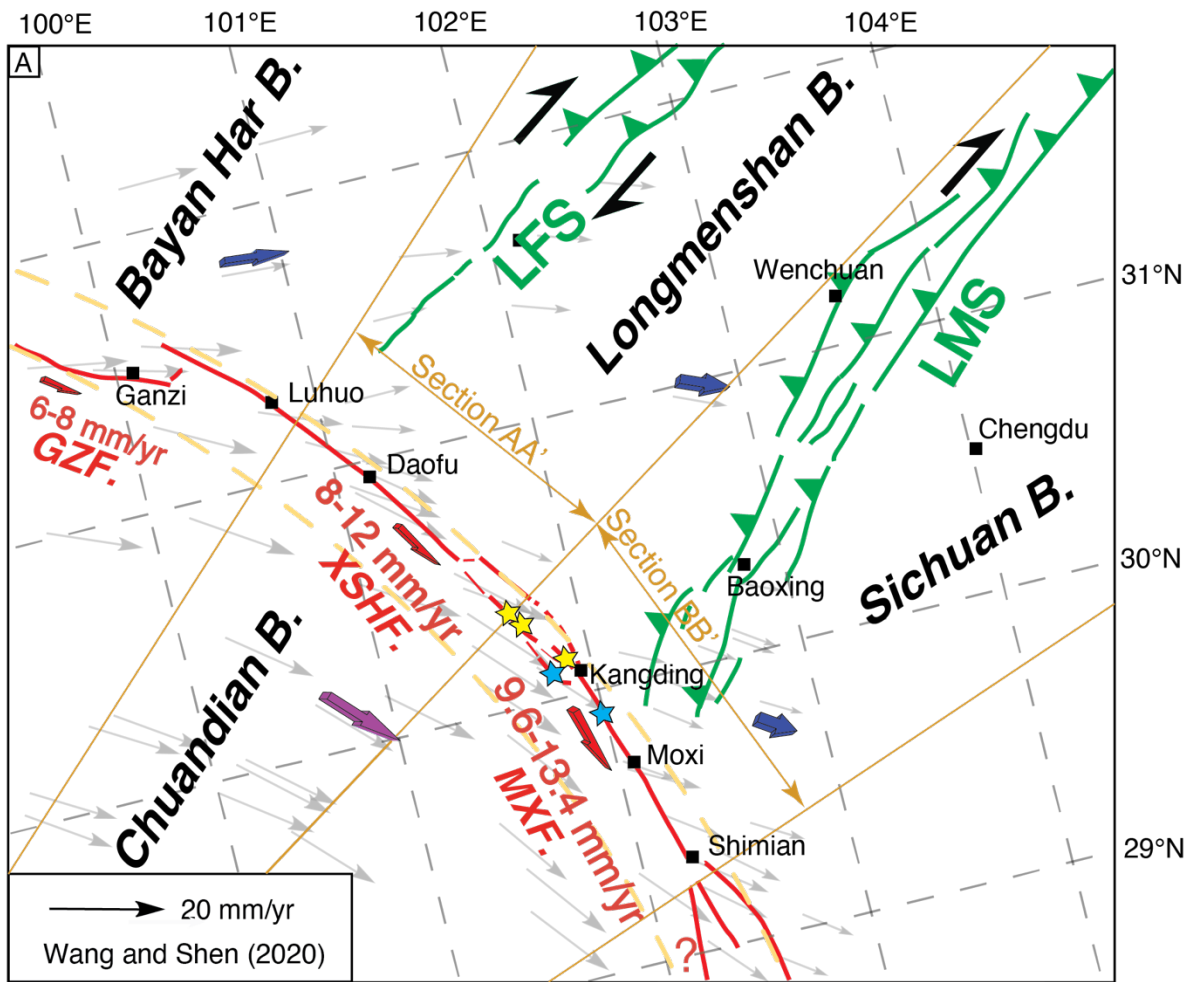
511 On one hand, Wang et al. (2020) proposed an elastic block model (Meade and Loveless,
512 2009) for SE Tibet that explains well the 15 years (1999-2014) of regional GPS data (Wang et al.,
513 2017), especially north of the Red River fault. They inferred a 11.8 ± 0.6 mm/yr slip rate along the
514 Ganzi fault, that increases to 14.5 ± 0.9 mm/yr (#10b in Fig. 3 and Table 1) along the XSH fault. The
515 late Quaternary rates that we propose ($6 - 8$ mm/yr for the Ganzi fault and $>8 - 12$ mm/yr for the SE
516 XSH fault) represent $\sim 70\%$ of these rates. This difference may be explained by the fact that the
517 block model considers that all deformation between the blocks is absorbed along the bounding
518 faults, while in fact a fraction of the deformation may also be absorbed by other smaller structures
519 within the blocks.

520 On the other hand, Wang and Shen (2020) proposed a GPS-derived deformation field for
521 most of continental China based on a 17 years-long dataset (1999-2016). They suggested that
522 deformation in Tibet, including in the XSH fault region, is mostly continuous and cannot be

523 described by the relative motion of minimally-deformed blocks. In that case, deformation is instead
524 quantified along velocity profiles. In order to see a clear trend in the rate evolution on both sides of
525 the fault, it is wise to not simply compare GNSS stations located on both sides of the fault, but to
526 make wide (~100 km) and long (>300 km) transects perpendicular to the fault. Profiles from Wang
527 and Shen (2020) show a slight along-strike increase of velocity from ~11 mm/yr across the
528 Yalahe/Selaha faults (section A-A' in Fig. 9A,B, #24a in Fig. 3 and Table 1), to ~13 mm/yr across
529 the Moxi fault (section B-B', #24b). While the limit between their sections AA' and BB' falls near
530 the Selaha Pass, these GPS estimates are still consistent with what we determined at the late
531 Quaternary timescale across these faults.

532 The most recent GPS datasets, analyzed in two different ways, both suggest a progressive
533 increase toward the SE of the left-lateral slip rate along the XSH fault, as we document in this study
534 at a much longer timescale. Similarly, the most recent InSAR study (Qiao and Zhou, 2021)
535 suggested an increase from 8.1 - 11.1 mm/yr along the NW XSH fault (#7b in Fig. 3 and Table 1),
536 to 8.8 - 16 mm/yr across the SE XSH fault (#7c), and 16.5 - 19.3 mm/yr along the Moxi fault (#7d).
537 Note however that the authors recognized that the latter rate may be overestimated due to
538 unwrapping and local atmospheric errors. A SE rate increase reaching at least Moxi town would be
539 in agreement with the observed eastward projected rate decrease observed from GPS vectors
540 relative to stable Eurasia (e.g., Wang and Shen, 2020) located north of the XSH fault system, from
541 the Bayan Har block to the Longmenshan block, as well as from the Longmenshan block to the
542 Sichuan Basin (Fig. 9A).

543



545 **Figure 9:** (A) Conceptual 2D model of Xianshuihe fault following India–Asia collision (modified
546 from Bai et al., 2018). Red arrows show southeastward slip rate increase, with rates from Chevalier
547 et al. (2017) along Ganzi fault (GZF), Bai et al. (2018) (yellow stars) and this study along
548 Xianshuihe/Selaha fault (XSHF), and this study along Moxi fault (MXF) (light blue stars).
549 LFS=Longriba fault system, LMS=Longmenshan. Orange dashed lines show small circles (with
550 pole of rotation in eastern Himalayan syntaxis) that best fits the overall trace of Xianshuihe fault
551 system. Grey arrows show GPS vectors relative to stable Eurasia (Wang and Shen, 2020) with
552 oblique orange lines representing extent of their fan-shaped sections AA' and BB' shown in (B).
553 Blue and purple 3D arrows show block movement on each side of Xianshuihe fault system with their
554 appropriate lengths according to GPS velocities. (B) Tangential (sinistral positive) components of
555 GPS velocity profiles modified from Wang and Shen (2020) (with respect to Eurasia) with maximum
556 rate across Xianshuihe and Moxi faults in green and purple, respectively. This is consistent with the
557 increase in slip rate between the two fault segments we suggest with our late Quaternary rates. (C)
558 Fault traces (thick colored lines) and strike directions (thin colored lines) of Xianshuihe fault.
559 Dashed black lines show ~25° clockwise bend between NW XSH and Moxi fault segments. Orange
560 dashed line follows a small circle along which motion would be purely strike-slip. Yellow arrows
561 represent directions of extension (Mugecuo pull-apart basin) and shortening (Moxi fault). Note that
562 extension and shortening rates are inferred based on strike-slip rates and fault geometry.
563 Earthquake hazard (and their estimated magnitude in red) is indicated by large orange stars (see
564 discussion in text).

565

566 **5.3 Example of a pull-apart basin within a restraining bend**

567 While the NW XSH fault has a single, linear and continuous trace striking N135°E for ~180
568 km, its geometry changes dramatically near the Huiyuansi Basin (N148°E), where it splits into the
569 four en-echelon faults discussed here (Yalahe-Selaha-Mugecuo-Zheduotang), before resuming as a
570 single fault trace striking N160°E (Moxi segment) (Figs. 2 and 9C). This ~25° clockwise bend has
571 been interpreted to have formed a restraining bend that would explain the very high elevations of
572 the Yala (peak at 5820 m) and Daxue (Gongga Shan peak at 7556 m) Ranges (Allen et al., 1991;
573 Burchfiel et al., 1995; Zhang et al., 2017). Zhang et al. (2017) interpreted the onset of rapid
574 exhumation (at a rate of ~1.85 mm/yr) of the Yala Range at ~9 Ma as corresponding to the
575 restraining bend initiation, and thus to the propagation of the XSH fault first along the Yalahe fault.
576 They then interpreted an exhumation rate decrease at ~4 Ma in the Yala Range as due to a slip rate

577 decrease along the Yalaha fault, and further activation of the Selaha and Zheduotang faults. This
578 resulted in a southward shift in the restraining bend from the Yala to the Daxue Range, where the
579 highest peaks are now located.

580 This mountain range indeed shows the fastest present-day erosion rates in the entire eastern
581 margin of the Tibetan Plateau, between 1.0 ± 0.4 and 7.6 ± 2.5 mm/yr, derived from ^{10}Be
582 concentrations in river sand (Ouimet et al., 2009; Cook et al., 2018) (orange contour in Fig. 2C).
583 Considering an average rate of ~ 3 mm/yr, Cook et al. (2018) estimated that such fast localized
584 exhumation has persisted since 3–4 Ma. While this timing is consistent with that proposed by Zhang
585 et al. (2017) using thermochronology, Cook et al. (2018) suggested that the geometry of the
586 restraining bend can only account for a fraction of the fast exhumation rate. Indeed, considering that
587 motion is purely strike-slip along the XSH fault, ~ 11.4 mm/yr (or 9.6–13.4 mm/yr) of left-lateral
588 slip along the Moxi segment (this study) in a 25° restraining bend between the XSH and Moxi
589 segments would imply a shortening rate of 4.8 ± 0.8 mm/yr across the Moxi segment in a planar
590 geometry (Fig. 9C). Such shortening may potentially explain the high exhumation rates in the
591 Daxue Range (Cook et al., 2018). However, the entire XSH fault system appears to follow a small
592 circle corresponding to a Euler rotation pole located in the eastern Himalayan syntaxis (25.0829°N ,
593 93.5747°E in Bai et al., 2018, Fig. 10A; 25.65°N , 94.31°E in Cook et al., 2018). Considering that
594 small circle as representing a direction of pure strike-slip motion, the bend then becomes $\sim 10^\circ$ (Fig.
595 9C), which would imply only 2.0 ± 0.3 mm/yr of compression across the Moxi fault, an amount too
596 small to solely explain the fast, present-day exhumation rates in the Daxue Range (Cook et al.,
597 2018). Sixty kilometers to the south, the Moxi fault splits into the Anninghe and Daliangshan faults
598 that left-laterally offset the Yangtze River by ~ 60 km (Wang et al., 1998) (near $\sim 27^\circ\text{N}$, Fig. 1). The
599 northern Anninghe fault striking $\text{N}185^\circ\text{E}$ implies another $\sim 25^\circ$ of clockwise rotation of the direction
600 of motion, hence another restraining bend (Fig. 1). However, that bend is located too far south to
601 explain the high erosion and very high elevations in the Gongga Shan region (Cook et al., 2018).

602 In this tectonic setting, subsidence in the Mugecuo area (Fig. 5A) is rather surprising in a

603 zone of high elevation and recent fast exhumation rates. The geometry of the SE Selaha and
604 Zheduotang faults is typical of a large-scale (~4.5 km-wide) pull-apart basin (Fig. 5A) in between
605 the Yala Range, where fast exhumation occurred between 9 and 4 Ma (Zhang et al., 2017), and the
606 Daxue Range, where very fast exhumation is occurring since ~4 Ma (Cook et al., 2018). Local
607 subsidence thus appears to be the consequence of strike-slip motion on the SE Selaha fault striking
608 N154° and the Zheduotang fault striking N148° (Figs. 9C and 10). The corresponding amount of
609 NW-SE extension within the Mugecuo pull-apart basin can thus be estimated by summing the rates
610 along these two bounding faults: 3.9 – 4.9 mm/yr for the SE Selaha fault at the YJG site (Bai et al.,
611 2018) and 3.4 - 4.8 mm/yr for the Zheduotang fault at the ZDT site (this study), thus a total of 7.3 –
612 9.7 mm/yr (Figs. 9C and 10). This value would correspond to that of the subsidence in the pull-apart
613 basin if every fault strand was vertical, and would thus yield an upper bound for the total vertical
614 motion.

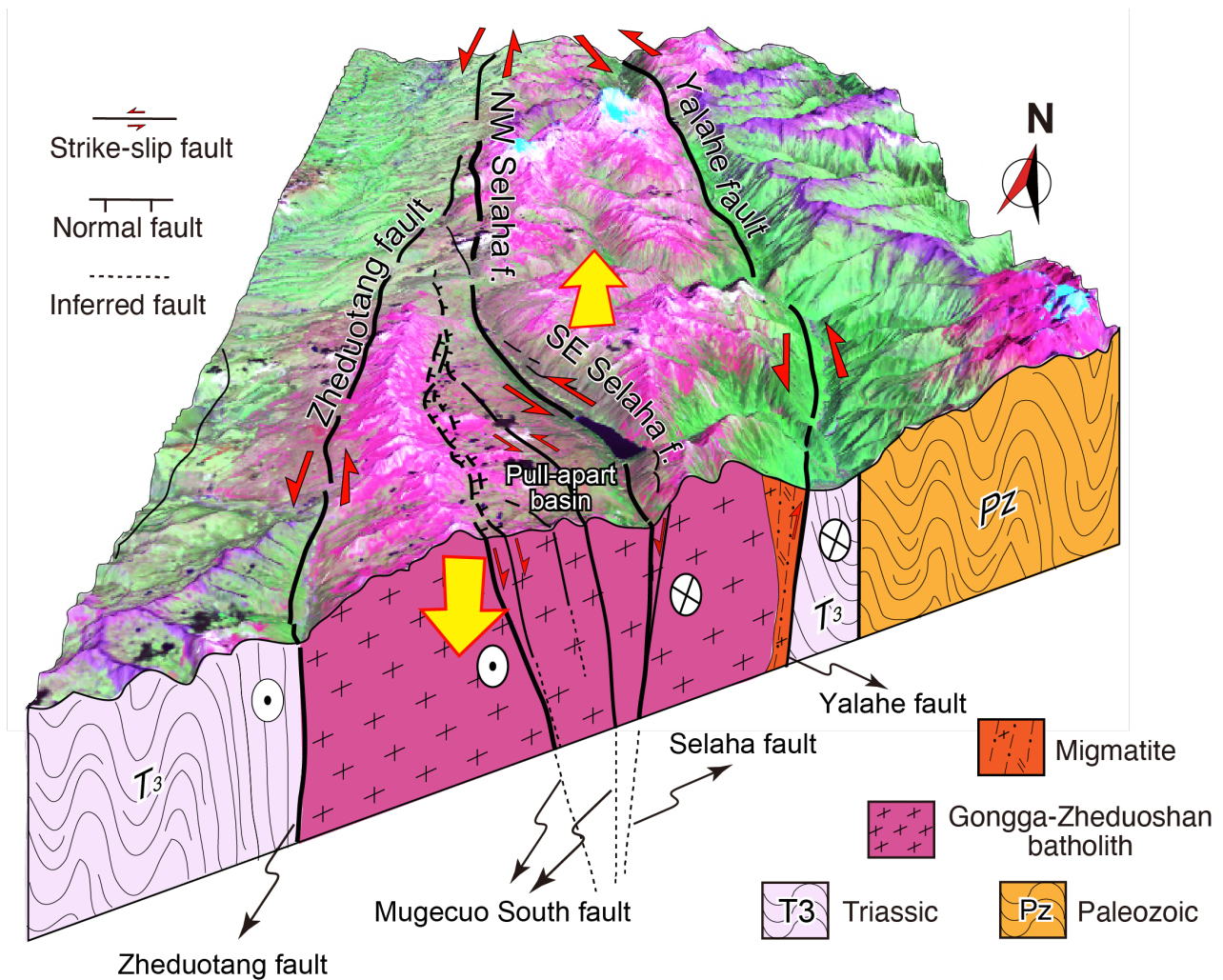
615 At such rate, the ~600 m-deep Mugecuo Lake depression (Fig. 5F) would form in 60 to 80
616 kyr. This only represents a first order estimate as it does not account for erosion nor the actual dip of
617 the faults (which remains to be constrained), which would increase the time required for the pull-
618 apart basin to form. In addition, in the pull-apart basin, vertical motion appears asymmetrical, with
619 a ~300 m higher topography and more numerous normal fault strands on the SW side compared to
620 that on the NE (Fig. 5F). This is consistent with much faster exhumation rates (determined from
621 cosmogenic ¹⁰Be basin-wide measurements) to the SW compared to the NE (orange vs green
622 contours, respectively, Fig. 2C) (Ouimet et al., 2009; Cook et al., 2018). However, the zone of
623 fastest exhumation is located ~30 km farther south (Cook et al., 2018) (Fig. 2C) and cannot be
624 explained by pull-apart kinematics alone. We thus interpret the Mugecuo zone as a pull-apart basin
625 within a larger restraining bend (see discussion above), which implies a complex 3D fault geometry
626 (Fig. 10) that has, to our knowledge, rarely been described.

627 A striking peculiarity of the Yalaha-Selaha-Mugecuo-Zheduotang segments is that they are
628 located where the XSH fault crosscuts a ~120 km-long granite batholith that formed during at least

629 four distinct magmatic episodes (obtained from U/Pb zircon ages): Triassic (Gongga granite, 216-
630 204 Ma), Middle Jurassic (Zheduo granite, ~170 Ma), Oligocene (~27 Ma) and Miocene (20-13
631 Ma) (Roger et al., 1995; Li and Zhang, 2013; Li et al., 2015; Searle et al., 2016). This batholith is
632 the only Cenozoic massif in all of SE Tibet, and crystallization ages as young as ~5 Ma have been
633 reported (Searle et al., 2016; Zhang et al., 2017). Ar/Ar ages are as young as 3.5 Ma (Wallis et al.,
634 2003; Zhang et al., 2004; Chen et al., 2006) and apatite fission track ages are as young as 1.2 Ma
635 (Xu and Kamp, 2000; Wilson et al., 2011; Zhang et al., 2017). Such very young ages imply a high
636 geothermal gradient that may be one of the contributing factors to the present-day fast exhumation
637 rates (Cook et al., 2018). Indeed, young magmatism and high heat flow may favor uplift. However,
638 young (≤ 5 Ma) granite bodies are rare and small in extent, so that it is challenging to quantify this
639 possible effect.

640 It is also surprising that the local trace of the faults at the surface is so complex where it
641 crosses the granite batholith, which is most likely more rigid than the surrounding Triassic flysch.
642 Indeed, farther north, where the Ganzi segment of the XSH fault system cuts and offsets the
643 Mesozoic Queer Range granite by 76–90 km (Wang and Burchfiel, 2000; Wang et al., 2009), the
644 fault trace is linear and does not appear to be affected by lithology (Fig. 1). Therefore, the key point
645 may thus be that the young age of the granite and/or the high regional heat flow concur to create the
646 high elevation of Gongga Shan. In addition, the high amount of precipitation along the SE Tibetan
647 Plateau topographic step, that possibly pre-dates the XSH fault, enhanced erosion thus uplift (Cook
648 et al., 2018).

649



650

651 **Figure 10:** 3D geomorphic model of Mugecuo South fault zone area (mostly normal, with minor
 652 left-lateral motion), which forms a large-scale pull-apart basin with Mugecuo Lake in its lowest
 653 point. Legend as in Figure 2. Top image is Landsat.

654

655 5.4 Seismic hazard in the Kangding region

656 Using the late Quaternary slip rates we determined in this study helps us calculate the
 657 current slip deficit since the last large earthquake occurred along a particular fault segment using
 658 empirical equations from Wells and Coppersmith (1994). Satellite image analyses and field
 659 investigation confirmed that at least the NW and central segments of the Yalaha fault are active with
 660 recent, as well as cumulative, offsets, while the potential activity along the SE part remains to be
 661 assessed. Taking a 0.6 - 2.2 mm/yr rate (as suggested for the NW part), a slip deficit of only 0.2 to
 662 0.7 m would have accumulated since the last large earthquake in 1700 (M7). This would correspond
 663 to a M_w 6.2 - 6.6 earthquake hazard at present (Wells and Coppersmith, 1994):

664 $M=6.69+0.74*\log(\text{maximum displacement of } 0.2 - 0.7 \text{ m}).$

665 The Selaha fault is regarded as a seismic gap, because the seismic energy released by the 2014
666 M_w 5.9 and 5.6 Kangding earthquake sequence is far less than the accumulated strain energy since
667 the 1955 M_w 7.5 earthquake on the Zheduotang fault (e.g., Jiang et al., 2015a; Xie et al., 2017). The
668 regional Coulomb stress increase following the 2008 Wenchuan (e.g., Parsons et al., 2008; Toda et
669 al., 2008; Shan et al., 2009; Nalbant and McCloskey, 2011) and 2013 Lushan (M_s 7.0) (Shan et al.,
670 2013; Yang et al., 2015; Guo et al., 2018) earthquakes implies that the seismic risk in the Kangding
671 region has increased. Coulomb stress evolution due to co-seismic dislocation and post-seismic
672 viscoelastic relaxation, and on time-dependent probabilistic risk models, both suggest that the
673 Selaha fault has a particularly high earthquake probability (e.g., Xu et al., 2013, 2019; Shao et al.,
674 2016).

675 At a more detailed level, the Selaha fault has especially been suggested as a seismic gap
676 because of the absence of large earthquakes since 1748 along its NW section, and 1725 along its SE
677 section, respectively, with a $M\sim 7$ earthquake risk at present (e.g., Allen et al., 1991; Wen, 2000;
678 Wen et al., 2008; Papadimitriou et al., 2004; Cheng et al., 2011; Shao et al., 2016; Bai et al., 2018;
679 Qiao and Zhou, 2021). However, our discovery of the Mugecuo South fault zone followed by our
680 recent field investigation revealed numerous normal fault strands with cumulative fault scarps up to
681 ~ 10 m high at places (Pan et al., 2020). Although the geometry of the fault is different from that of
682 the more linear and continuous traces of the Yalahe and Zheduotang faults, the numerous fault
683 strands at the surface may connect at depth. Because the Selaha and Mugecuo South faults together
684 form a large-scale pull-apart basin bounded by numerous normal fault strands, the pull-apart may
685 rupture more easily (Segall and Pollard, 1980; Li et al., 2015). We thus suggest that large
686 earthquakes may more easily occur in the zone of the Mugecuo pull-apart basin, compared to other
687 sections of the Selaha fault. As the slip rate along the Mugecuo South fault is still unknown, taking
688 that of the NW or SE Selaha fault (~ 9.75 and $3.9 - 4.9$ mm/yr, respectively), would yield a slip
689 deficit of ~ 2.8 or $1.2-1.5$ m, respectively, since 1725. This would correspond to a potential

690 earthquake as high as $\sim M_w 6.7 - 7.0$ at present ($M = 6.69 + 0.74 * \log[\text{maximum displacement of 2.8}$
691 m], Wells and Coppersmith, 1994).

692 Similarly, taking our 9.6 - 13.4 mm/yr rate along the Moxi fault would correspond to a slip
693 deficit of 2.3 - 3.2 m since the last large ($M_{7.4}$) earthquake in 1786, i.e., a potential earthquake of
694 $M_w 7.0-7.1$ at present, consistent with what Qiao and Zhou (2021) determined ($M_w 7.37$) using an
695 elastic dislocation model. Those authors also determined that the return time of characteristic large
696 earthquakes ($M_w 7.25$) along the Moxi fault is 155 years. The fact that the last large earthquake
697 occurred 235 years ago may thus suggest that an earthquake is overdue along that segment hence a
698 high seismic risk. This would devastate Moxi town, which, despite currently being less populated
699 than Kangding city, continuously expands to cater to increasing tourism, thanks to its location at the
700 base of Gongga Shan.

701

702 **6. Conclusion**

703 By studying four locations along the four en-echelon faults of the SE Xianshuihe fault:

704 (1) We quantitatively determined that the late Quaternary slip rate along the Zheduotang fault is 3.4
705 – 4.8 mm/yr.

706 (2) We discovered a new fault zone (Mugecuo South) between the SE Selaha and Zheduotang
707 faults, along which numerous, mostly normal, fault strands with cumulative scarps up to ~ 10 m
708 exist. Due to the fresh nature of the scarps, we infer that the 1725 $M 7.0$ earthquake may have
709 occurred along that particular fault zone. This new fault segment forms a large-scale pull-apart
710 basin causing subsidence of the Mugecuo Lake zone.

711 (3) The Mugecuo pull-apart basin is located in a zone of exceptionally high elevation (culminating
712 in Gongga Shan, 7556 m) due to the large-scale restraining bend along the Xianshuihe fault,
713 possibly in conjunction with high heat flow and intense erosion.

714 (4) We suggest from field investigation that the central part of the Yalahe fault is active, with clear
715 fault scarps that can be followed for ~ 10 km. While slip rates are still lacking, we suggest that it

716 most likely also contributes to the total slip rate of the SE Xianshuihe fault.

717 (5) We determined that SE of Kangding, the late Quaternary slip rate along the Moxi fault ranges
718 from 9.6 to 13.4 mm/yr.

719 (6) The slip rate along the Xianshuihe fault system thus increases to the SE from 6-8 mm/yr along
720 the Ganzi fault, to 8-11 mm/yr along the NW Xianshuihe fault, to 8-12 mm/yr along the SE
721 Xianshuihe fault, to 9.6-13.4 mm/yr along the Moxi fault.

722 (7) We suggest that high seismic hazard exists in the SE Xianshuihe fault, especially in the
723 Mugecuo pull-apart basin, which may facilitate earthquake nucleation.

724

725 **Acknowledgments**

726 This work was financially supported by the National Natural Science Foundation of China [NSFC
727 42020104007, 41941016, 4191101281], the China Geological Survey [DD20190059], the Key
728 Special Project for Introduced Talents Team of Southern Marine Science and Engineering
729 Guangdong Laboratory (Guangzhou) (GML2019ZD0201), the Ministry of Science and Technology,
730 China (2021FY100101, 2019QZKK0901). We thank Editor T. Schildgen and the Associate Editor,
731 as well as Alex Densmore and two anonymous reviewers for their constructive comments. All
732 geochronology data are in Table 2 and can be downloaded online
733 (<https://zenodo.org/record/5108951#.YPDufy0RrjA>).

734

735 **References**

- 736 Allen, C.R., Luo, Z., Qian, H., Wen X., Zhou, H., & Huang, W. (1991). Field study of a highly
737 active fault zone: The XSF of southwestern China. *Geological Society of America Bulletin*,
738 *103*, 1178–1199. Doi:10.1130/0016-7606(1991)103<1178:FSOAHA>2.3.CO;2
- 739 Bai, M., Chevalier, M.L., Pan, J., Replumaz, A., Leloup, P.H., Métois, M., & Li, H. (2018).
740 Southeastward increase of the late Quaternary slip-rate of the Xianshuihe fault, eastern Tibet.
741 Geodynamic and seismic hazard implications. *Earth and Planetary Science Letters*, *485*, 19-

- 742 31. Doi:10.1016/j.epsl.2017.12.045
- 743 Balco, G., Stone, J.O., Lifton, N. A., & Dunai, T.J. (2008). A complete and easily accessible means
744 of calculating surface exposure ages or erosion rates from ^{10}Be and ^{26}Al measurements.
745 *Quaternary Geochronology*, 3, 174-195. Doi:10.1016/j.quageo.2007.12.001
- 746 Bevington, P.R., & Robinson, D.K. (2002). Data reduction and error analysis for the physical
747 sciences. 336pp, McGraw-Hill
- 748 Burchfiel, B.C., Chen, Z., Liu, Y., & Royden, L.H. (1995). Tectonics of the Longmen Shan and
749 adjacent regions. *International Geology Review*, 37, 661–736
- 750 Chen, W., Tan, Q., Wen, P., & Liang, X. (1985). Geological map of Kangding (H-47-18). Sichuan
751 Institute of Geology and Mineral Resources, Scale 1/200,000
- 752 Chen, W., Zhang, Y., Zhang, Y.Q., Jin, G.S., & Wang, Q.L. (2006). Late Cenozoic episodic uplifting
753 in southeastern part of the Tibetan plateau-evidence from Ar–Ar thermochronology. *Acta*
754 *Geologica Sinica*, 22, 867–872. Doi:10.3969/j.issn.1000-0569.2006.04.010 (in Chinese)
- 755 Chen, G., Xu, X., Wen, X., & Wang, Y. (2008). Kinematical transformation and slip partitioning of
756 northern to eastern active boundary belt of Sichuan-Yunnan block. *Seismology and Geology*,
757 30, 58-85 (in Chinese)
- 758 Chen, G., Xu, X., Wen, X., & Chen, Y. (2016). Late Quaternary slip-rates and slip-partitioning on
759 the southeastern Xianshuihe fault system, Eastern Tibetan Plateau. *Acta Geologica Sinica*, 90,
760 537-554. Doi:10.1111/1755-6724.12689
- 761 Cheng, J., Liu, J., Gan, W., Yu, H., & Li, G. (2011). Characteristics of strong earthquake evolution
762 around the eastern boundary faults of the Sichuan-Yunnan rhombic block. *Science China–*
763 *Earth Sciences*, 54, 1716–1729. Doi:10.1007/s11430-011-4290-2
- 764 Chevalier, M.L., Ryerson, F.J., Tapponnier, P., Finkel, R., Van der Woerd, J., Li, H., & Liu, Q.
765 (2005). Slip-rate measurements on the Karakorum fault may imply secular variations in fault
766 motion. *Science*, 307(5708), 411–414. Doi: 10.1126/science.1105466
- 767 Chevalier, M.L., Hilley, G., Tapponnier, P., Van Der Woerd, J., Liu-Zeng, J., Finkel, R.C., Ryerson,

768 F.J., Li, H., & Liu, X. (2011). Constraints on the late Quaternary glaciations in Tibet from
769 cosmogenic exposure ages of moraine surfaces. *Quaternary Science Reviews*, 30, 528–554.
770 Doi:10.1016/j.quascirev.2010.11.005

771 Chevalier, M.L., Van der Woerd, J., Tapponnier, P., Li, H., Ryerson, F.J., & Finkel, R.C. (2016).
772 Late Quaternary slip-rate along the central Bangong-Chaxikang segment of the Karakorum
773 fault, western Tibet; *Geological Society of America Bulletin*, 128, 284-314,
774 doi:10.1130/B31269.1.

775 Chevalier, M.L., Leloup, P.H., Replumaz, A., Pan, J., Metois, M., & Li, H. (2017). Temporally
776 constant slip-rate along the Ganzi fault, NW Xianshuihe fault system, eastern Tibet.
777 *Geological Society of America Bulletin*, 130(3/4), 396–410. Doi:10.1130/B31691.1

778 Chevalier, M. L., & Replumaz, A. (2019). Bimodal climatic signal for glaciations in SE Tibet:
779 Marine Isotope Stages 2 and 6. *Earth and Planetary Science Letters*, 507, 105-118.
780 Doi:10.1016/j.epsl.2018.11.033

781 CEA: China Earthquake Administration, Earthquake Disaster Prevention Department. Catalogue of
782 strong earthquakes in Chinese history. *Beijing Seismological Press*, 1995.

783 Cook, K.L., Hovius, N., Wittmann, H., Heimsath, A.M., & Lee, Y. (2018). Causes of rapid uplift
784 and exceptional topography of Gongga Shan on the eastern margin of the Tibetan Plateau.
785 *Earth and Planetary Science Letters*, 481, 328–337, doi: 10.1016/j.epsl.2017.10.043

786 Dai, F.C., Lee, C.F., Deng, J.H., & Tham, L.G. (2005). The 1786 earthquake-triggered landslide dam
787 and subsequent dam-break flood on the Dadu River, southwestern China. *Geomorphology*, 65,
788 205–221. Doi:10.1016/j.geomorph.2005.06.011

789 Deng, Q., Zhang, P., Ran, Y., Yang, X., Min, W., & Chu, Q. (2003). Basic characteristics of active
790 tectonics of China. *Science in China*, 46, 356–372. Doi:10.1360/03yd9032

791 Friedrich, A.M., Wernicke, B.P., Niemi, N.A., Bennett, R.A., & Davis, J.L. (2003). Comparison of
792 geodetic and geologic data from the Wasatch region, Utah, and implications for the spectral
793 character of Earth deformation at periods of 10 to 10 million years. *Journal of Geophysical*

794 *Research*, 108(B4), 2199. Doi:10.1029/2001JB000682

795 Gan, W., Zhang, P., Shen, Z., Niu, Z., Wang, M., Wan, Y., Zhou, D., & Cheng, J. (2007). Present-
796 day crustal motion within the Tibetan Plateau inferred from GPS measurements. *Journal of*
797 *Geophysical Research*, 112, B08416. Doi:10.1029/2005JB004120

798 Gosse, J., & Phillips, F. (2001). Terrestrial in situ cosmogenic nuclides: Theory and application.
799 *Quaternary Science Reviews*, 20, 475–1560. Doi:10.1016/S0277-3791(00)00171-2

800 Guo, R., Zheng, Y., Tian, W., Xu, J., & Zhang, W. (2018). Locking Status and Earthquake Potential
801 Hazard along the Middle-South Xianshuihe Fault. *Remote sensing*, 10, 2048.
802 doi:10.3390/rs10122048

803 Hallet, B., & Putkonen, J. (1994). Surface dating of dynamic landforms: young boulders on aging
804 moraines. *Science*, 265, 937-940. Doi: 10.1126/science.265.5174.937

805 Han, S., Li, H., Pan, J., Lu, H., Zheng, Y., Liu, D., & Ge, C., (2019). Co-seismic surface ruptures
806 in Qiangtang Terrane: Insight into Late Cenozoic deformation of central Tibet.
807 *Tectonophysics*, 750, 359–378. Doi :10.11016/j.tecto.2018.11.001

808 Heyman, J., Stroeven, A.P., Harbor, J., & Caffee, M.W. (2011). Too young or too old: Evaluating
809 cosmogenic exposure dating based on an analysis of compiled boulder exposure ages. *Earth*
810 *and Planetary Science Letters*, 302, 71–80. Doi:10.1016/j.epsl.2010.11.040

811 Heyman, J. (2014). Paleoglaciation of the Tibetan Plateau and surrounding mountains based on
812 exposure ages and ELA depression estimates. *Quaternary Science Reviews*, 91, 30–41.
813 Doi:10.1016/j.quascirev.2014.03.018

814 Ji, L., Zhang, W., Liu, C., Zhu, L., Xu, J., & Xu, X. (2020). Characterizing interseismic deformation
815 of the Xianshuihe fault, eastern Tibetan Plateau, using Sentinel-1 SAR images. *Advances in*
816 *Space Research*, 66, 378–394. Doi:10.1016/j.asr.2020.03.043

817 Jiang, G., Wen, Y., Liu, Y., Xu, X., Fang, L., Chen, G., Meng, G., & Xu, C. (2015a). Joint analysis
818 of the 2014 Kangding, southwest China, earthquake sequence with seismicity relocation and
819 InSAR inversion. *Geophysical Research Letters*, 42, 3273-3281. Doi:10.1002/2015GL063750

820 Jiang, G., Xu, X., Chen, G., Liu, Y., Fukahata, Y., Wang, H., Yu, G., Tan, X., & Xu, C. (2015b).
821 Geodetic imaging of potential seismogenic asperities on the Xianshuihe-Anninghe-Zemuhe
822 fault system, southwest China, with a new 3-D viscoelastic interseismic coupling model.
823 *Journal of Geophysical Research - Solid Earth*, 120, 1855–1873. Doi:10.1002/2014JB011492

824 Kohl, C.P., & Nishiizumi, K. (1992). Chemical isolation of quartz for measurement of in-situ -
825 produced cosmogenic nuclides. *Geochimica et Cosmochimica Acta*, 56, 3583-3587.
826 Doi:10.1016/0016-7037(92)90401-4

827 Lal, D. (1991). Cosmic-ray labeling of erosion surfaces-In situ nuclide production rates and erosion
828 models. *Earth and Planetary Science Letters*, 104 (2-4), 424–439. Doi:10.1016/0012-
829 821X(91)90220-C

830 Li, Y., & Bürgmann, R. (2021). Partial coupling and earthquake potential along the Xianshuihe
831 Fault, China. *Journal of Geophysical Research*, doi:10.1029/2020JB021406

832 Li, T., Du, Q., Zhang, C., & You, Z., 1997. The Active Xianshuihe Fault Zone and its Seismic
833 Risk Assessment. Chengdu Cartographic Publishing House, Chengdu, 230 pp. (in
834 Chinese)

835 Li, H., & Zhang, Y. (2013). Zircon U–Pb geochronology of the Konggar granitoid and migmatite:
836 constraints on the Oligo-Miocene tectono-thermal evolution of the Xianshuihe fault zone, East
837 Tibet. *Tectonophysics*, 606, 127–139. Doi:10.1016/j.tecto.2013.07.007

838 Li, Z., Xiao, H., & Zhou, B. (2015). Effect of fault steps on propagation and termination behavior of
839 strike-slip earthquake surface rupture. *Seismology and Geology*, 37(1), 126-138 (in Chinese)

840 Li, T., Zhu, Y., Yang, Y., Xu, Y., An, Y., Zhang, Y., Feng, S., Huai, Y., & Yang, J. (2019). The current
841 slip rate of the Xianshuihe fault zone calculated using multiple observation data of crustal
842 deformation. *Chinese Journal of Geophysics*, 62(4), 1323-1335 (in Chinese)

843 Li J., Zhou, B., Li, T., Yang, Y., & Li, Z. (2020). Locking depth, slip rate, and seismicity distribution
844 along the Daofu–Kangding segment of the Xianshuihe fault system, eastern Tibetan Plateau.
845 *Journal of Asian Earth Sciences*, 193, 104328. Doi:10.1016/j.jseaes.2020.104328

- 846 Liang, M., Chen, L., Ran, Y., Li, Y., Wang, D., Gao, S., Han, M., & Zeng, D. (2020). Late
847 Quaternary activity of the Yalaha fault of the Xianshuihe fault zone, eastern margin of the
848 Tibet Plateau. *Seismology and Geology*, 42(2), 513-525. doi:10.3969/j.issn.0253-
849 4967.2020.02.016 (in Chinese)
- 850 Lifton, N., Sato, T., & Dunai, T.J. (2014). Scaling in situ cosmogenic nuclide production rates using
851 analytical approximations to atmospheric cosmic-ray fluxes. *Earth and Planetary Science*
852 *Letters*, 386, 149-160. Doi:10.1016/j.epsl.2013.10.052.
- 853 Lin, B., Chen, T., Pu, X., Liu, W., & Peng, M. (1986). Rupture processes of strong earthquakes on
854 Xianshuihe fault belt and seismic activity. *Acta Seismologica Sinica*, 8(1), 1–20. (in Chinese)
- 855 Lisiecki, L.E., & Raymo, M.E. (2005). A Pliocene–Pleistocene stack of 57 globally distributed
856 benthic $\delta^{18}\text{O}$ records. *Paleoceanography*, 20, PA1003. Doi:10.1029/2004PA001071
- 857 Liu, Z., Zhang, G., Hu, Y., & Yang, Y. (1977). Geological map of Gongga (H-47-24). Sichuan
858 Institute of Geology, Scale 1/200,000
- 859 Lu, Y., Shi, R., Hu, Y., & Zhang, S. (1975). Geological map of Yingjing (H-48-19). Sichuan
860 Institute of Geology, Scale 1/200,000
- 861 Meade, B. J., & Loveless, J. P. (2009). Block modeling with connected fault network geometries
862 and a linear elastic coupling estimator in spherical coordinates. *Bulletin of the Seismological*
863 *Society of America*, 99 (6), 3124–3139. Doi:10.1785/0120090088
- 864 Nalbant, S.S., & McCloskey, J. (2011). Stress evolution before and after the 2008 Wenchuan, China
865 earthquake. *Earth and Planetary Science Letters*, 307, 222–232.
866 Doi:10.1016/j.epsl.2011.04.039
- 867 Ouimet, W.B., Whipple, K.X., & Granger, D.E. (2009). Beyond threshold hillslopes: chan-nel
868 adjustment to base-level fall in tectonically active mountain ranges. *Geology* 37, 579–582.
869 Doi:10.1130/g30013a.1
- 870 Pan, J., Li, H., Chevalier, M.L., Bai, M., Liu, F., Liu, D., Zheng, Y., Lu, H., & Zhao, Z. (2020). A
871 newly discovered active fault on the Selaha-Kangding segment along the SE Xianshuihe fault:

- 872 the South Mugecuo fault. *Acta Geologica Sinica*, 94(11), 3178-3188 (in Chinese). doi:
873 10.19762/j.cnki.dizhixuebao.2020196
- 874 Papadimitriou, E., Wen, X., Karakostas, V., & Jin, X. (2004). Earthquake Triggering along the
875 Xianshuihe Fault Zone of Western Sichuan, China. *Pure applied Geophysics*, 161, 1683–1707.
876 Doi:10.1007/s00024-003-2471-4
- 877 Parsons, T., Ji, C., & Kirby, E. (2008). Stress changes from the 2008 Wenchuan earthquake and
878 increased hazard in the Sichuan basin. *Nature*, 454, 509–510. Doi:10.1038/nature07177
- 879 Putkonen, J., & Swanson, T. (2003). Accuracy of cosmogenic ages for moraines. *Quaternary*
880 *Research*, 59, 255–261. Doi:10.1016/S0033-5894(03)00006-1.
- 881 Qiao, X., & Zhou, Y. (2021). Geodetic imaging of shallow creep along the Xianshuihe fault and its
882 frictional properties. *Earth and Planetary Science Letters*, 567, 117001.
883 Doi:10.1016/j.epsl.2021.117001
- 884 Roger, F., Calassou, S., Lancelot, J., Malavieille, J., Mattauer, M., Xu, Z., Hao, Z., & Hou, L.
885 (1995). Miocene emplacement and deformation of the Konga Shan granite (Xianshui He fault
886 zone, west Sichuan, China): Geodynamic implications. *Earth and Planetary Science Letters*,
887 130, 201–216. Doi:10.1016/0012-821X(94)00252-T
- 888 Searle, M.P., Roberts, N.M.W., Chung, S.-L., Lee, Y., Cook, K.L., Elliott, J.R., Weller, O.M., St-
889 Onge, M.R., Xu, X.-W., Tan, X.-B., & Li, K. (2016). Age and anatomy of the Gongga Shan
890 batholith, eastern Tibetan Plateau, and its relationship to the active Xianshuihe fault.
891 *Geosphere*, 12 (3), 948–970. Doi:10.1130/ges01244.1
- 892 Segall, P., & Pollard, D. (1980). Mechanics of Discontinuous Faults. *Journal of*
893 *Geophysical Research*, 85(B8), 4337-4350
- 894 Shao, Z., Xu, J., Ma, H., & Zhang, L. (2016). Coulomb stress evolution over the past 200 years and
895 seismic hazard along the Xianshuihe fault zone of Sichuan, China. *Tectonophysics*, 670, 48-65.
896 Doi:10.1016/j.tecto.2015.12.018
- 897 Shan, B., Xiong, X., Zheng, Y., & Diao, F. (2009). Stress changes on major faults caused by Mw7.9

- 898 Wenchuan earthquake May 12, 2008. *Science in China*, 52, 593–601
- 899 Shan, B., Xiong, X., Zheng, Y., Jin, B., Liu, C., Xie, Z., & Hsu, H. (2013). Stress changes on major
900 faults caused by 2013 Lushan earthquake and its relationship with 2008 Wenchuan earthquake.
901 *Science in China - Earth Science*, 56, 1169-1176. Doi:10.1007/s11430-013-4642-1
- 902 Shen, Z., Lu, J., Wang, M., & Bürgmann, R. (2005). Contemporary crustal deformation around the
903 southeast borderland of the Tibetan Plateau. *Journal of Geophysical Research*, 110, B11409.
904 Doi:10.1029/2004JB003421
- 905 Stone, J. O. (2000). Air pressure and cosmogenic isotope production. *Journal of Geophysical*
906 *Research*, 105(B10), 23,753–23,759. Doi:10.1029/2000JB900181
- 907 Tapponnier, P., & Molnar, P. (1977). Active faulting and Cenozoic tectonics of China. *Journal of*
908 *Geophysical Research*, 82, 2905-2930. Doi:10.1029/JB082i020p02905
- 909 Toda, S., Lin, J., Meghraoui, M., & Stein, R.S. (2008). 12 May 2008 M = 7.9 Wenchuan, China,
910 earthquake calculated to increase failure stress and seismicity rate on three major fault systems.
911 *Geophysical Research Letters*, 35, L17305. Doi:10.1029/2008GL034903
- 912 Wallis, S., Tsujimori, T., Aoya, M., Kawakami, T., Terada, K., Suzuki, K., & Hyodo, H. (2003).
913 Cenozoic and Mesozoic metamorphism in the Longmenshan orogen: implications for
914 geodynamic models of eastern Tibet. *Geology*, 31, 745–748. Doi:10.1130/g19562.1
- 915 Wang, E., Burchfiel, B. C., Royden, L. H. Chen, L., Chen, J., Li, W., & Chen, Z. (1998). The
916 Cenozoic Xianshuihe– Xiaojiang, Red River, and Dali fault systems of southwestern Sichuan
917 and central Yunnan, China. *Geological Society of America Special Paper*, 327, 108p.
918 Doi:10.1130/SPE327
- 919 Wang, E., & Burchfiel, B.C. (2000). Late Cenozoic to Holocene deformation in southwestern
920 Sichuan and adjacent Yunnan, China, and its role in formation of the southeastern part of the
921 Tibetan Plateau. *Geological Society of America Bulletin*, 112, 413–423. Doi:10.1130/0016-
922 7606(2000)112<413:LCTHDI>2.0.CO;2
- 923 Wang, H., Wright, T.J., & Biggs, J. (2009). Interseismic slip rate of the northwestern Xianshuihe

- 924 fault from InSAR data. *Geophysical Research Letters*, 36, L03302.
- 925 Doi:10.1029/2008GL036560
- 926 Wang, S., Jiang, G., Xu, T., Tian, Y., Zheng, D., & Fang, X. (2012). The Jinhe–Qinghe fault—
927 An inactive branch of the Xianshuihe–Xiaojiang fault zone, Eastern Tibet. *Tectonophysics*, 544-
928 545, 93-102. Doi:10.1016/j.tecto.2012.04.004
- 929 Wang, W., Qiao, X., Yang, S., & Wang, D. (2017). Present-day velocity field and block kinematics
930 of Tibetan Plateau from GPS measurements. *Geophysical Journal International*, 208, 1088-
931 1102. Doi:10.1093/gji/ggw445
- 932 Wang, Y., Wang, M., & Shen, Z. (2017). Block-like versus distributed crustal deformation around
933 the northeastern Tibetan plateau. *Journal of Asian Earth Sciences*, 140, 31-47.
934 Doi:10.1016/j.jseaes.2017.02.040
- 935 Wang, W., Qiao, X., & Ding, K. (2020). Present-day kinematics in southeastern Tibet inferred from
936 GPS measurements. *Journal of Geophysical Research*, e2020JB021305.
937 Doi:10.1029/2020JB021305
- 938 Wang, M., & Shen, Z. (2020). Present-day crustal deformation of continental China derived from
939 GPS and its tectonic implications. *Journal of Geophysical Research*, 125, e2019JB018774.
940 Doi:10.1029/2019JB018774
- 941 Wells, D.L., & Coppersmith, K.J. (1994). New empirical relationships among magnitude, rupture
942 length, rupture width, rupture area, and surface displacement. *Bulletin of the Seismological*
943 *Society of America*, 84, 974–1002
- 944 Wen, X. (2000). Character of rupture segment of Xianshuihe- Zemuhe–Anninghe fault zone,
945 western Sichuan. *Seismology and Geology*, 22, 239–249
- 946 Wen, X., Ma, S., Xu, X., & He, Y. (2008). Historical pattern and behavior of earthquake ruptures
947 along the eastern boundary of the Sichuan–Yunnan faulted-block, southwestern China. *Physics*
948 *of the Earth and Planetary Interiors*, 168 (1–2), 16–36. Doi:10.1016/j.pepi.2008.04.013
- 949 Wilson, C.J.L., & Fowler, A.P. (2011). Denudational response to surface uplift in east Tibet:

950 evidence from apatite fission-track thermochronology. *Geological Society of America Bulletin*,
951 123, 1966–1987. Doi:10.1130/b30331.1

952 Xie, Z., Zheng, Y., Liu, C., Shan, B., Riaz, M. S., & Xiong, X. (2017). An integrated analysis of
953 source parameters, seismogenic structure, and seismic hazards related to the 2014 M S 6.3
954 Kangding earthquake, China. *Tectonophysics*, 712, 1-9. Doi:10.1016/j.tecto.2017.04.030

955 Xu, G., & Kamp, P.J.J. (2000). Tectonics and denudation adjacent to the Xianshuihe Fault, eastern
956 Tibetan Plateau: constraints from fission track thermochronology. *Journal of Geophysical*
957 *Research*, 105, 19231–19251. Doi:10.1029/2000jb900159

958 Xu, J., Shao, Z., Ma, H., & Zhang, L. (2013). Evolution of Coulomb stress and stress interaction
959 among strong earthquakes along the Xianshuihe fault zone. *Chinese Journal of Geophysics*,
960 56(4), 1146-1158 (in Chinese). Doi:10.6038/cjg20130410

961 Xu, J., Shao, Z., Liu, J., & Ji, L. (2019). Coulomb stress evolution and future earthquake
962 probability along the eastern boundary of the Sichuan-Yunnan block. *Chinese Journal of*
963 *Geophysics*, 62(11), 4189-4213 (in Chinese)

964 Yan, B., & Lin, A. (2015). Systematic deflection and offset of the Yangtze River drainage system
965 along the strike-slip Ganzi-Yushu-Xianshuihe Fault Zone, Tibetan Plateau. *Journal of*
966 *Geodynamics*, 87, 13-25. Doi:10.1016/j.jog.2015.03.002

967 Yan, B., & Lin, A. (2017). Holocene Activity and Paleoseismicity of the Selaha Fault, Southeastern
968 Segment of the Strike-Slip Xianshuihe Fault Zone, Tibetan Plateau. *Tectonophysics*, 694(2),
969 302–318. Doi:10.1016/j.tecto.2016.11.014

970 Yan, B., Jia, D., & Lin, A. (2018). Late Pleistocene-Holocene tectonic landforms developed along
971 the strikeslip Xianshuihe Fault Zone, Tibetan Plateau, China. *Journal of Geodynamics*, 120,
972 11–22. Doi:10.1016/j.jog.2018.05.005

973 Yan, B., Wang, M., Jia, D., & Cui, J. (2019). Investigation and magnitude re-evaluation of the 1955
974 Zheduotang earthquake, eastern Tibetan Plateau, China. *Geological Journal*, 2019, 1–13.
975 Doi:10.1002/gj.3628

- 976 Yang, W., Cheng, J., Liu, J., & Zhang, X. (2015). The Kangding earthquake swarm of November,
977 2014. *Earthquake Science*, 28(3), 197-207. Doi:10.1007/s11589-015-0123-2
- 978 Zechar, J.D., & Frankel, K.L. (2009). Incorporating and reporting uncertainties in fault slip rates.
979 *Journal of Geophysical Research*, 114, B12407. Doi:10.1029/2009JB006325
- 980 Zhang, Y., Chen, W., & Yang, N. (2004). ⁴⁰Ar/³⁹Ar dating of shear deformation of the Xianshuihe
981 fault zone in west Sichuan and its tectonic significance. *Science in China*, 47, 794–803.
982 Doi:10.1360/03yd0509
- 983 Zhang, P.Z. (2013). A review on active tectonics and deep crustal processes of the Western Sichuan
984 region, eastern margin of the Tibetan Plateau. *Tectonophysics*, 584, 7-22.
985 Doi:10.1016/j.tecto.2012.02.021
- 986 Zhang, Y., Replumaz, A., Leloup, P.H., Wang, G., Bernet, M., van der Beek, P., Paquette, J.L. &
987 Chevalier, M. L. (2017). Cooling history of the Gongga batholith: implications for the
988 Xianshuihe Fault and Miocene kinematics of SE Tibet. *Earth and Planetary Science Letters*,
989 465, 1-15. Doi:10.1016/j.epsl.2017.02.025
- 990 Zhang, L., Cao, D., Zhang, J., & Sui, L. (2019). Interseismic Fault Movement of Xianshuihe Fault
991 Zone Based on Across-Fault Deformation Data and InSAR. *Pure and Applied Geophysics*,
992 176, 649–667. Doi:10.1007/s00024-018-1989-4
- 993 Zheng, G., Wang, H., Wright, Tim J., Lou, Y., Zhang, R., Zhang, W., Shi, C., Huang, J., & Wei, N.
994 (2017). Crustal deformation in the India-Eurasia collision Zong from 25 years of GPS
995 measurements. *Journal of Geophysical Research*, 122, 9290–9312.
996 Doi:10.1002/2017JB014465
- 997 Zhou, R., He, Y., Huang, Z., Li, X., & Yang, Z. (2001). The slip rate and recurrence of strong
998 earthquakes of Qianning-Kangding segment, the Xianshuihe fault zone. *Acta Seismologica*
999 *Sinica*, 23(3), 250-261 (in Chinese)